Simplified design of bridges for multiple-support earthquake excitation

Savvas P. Papadopoulos [a] and Anastasios G. Sextos [b]

[a] Civil Engineer, Ph.D. Candidate, Division of Structural Engineering, Department of Civil Engineering, Aristotle University Thessaloniki, Greece; e-mail: savvaspp@civil.auth.gr

[b] Professor, Department of Civil Engineering, University of Bristol, UK (a.sextos@bristol.ac.uk)

(*Corresponding Author)

ABSTRACT

This paper presents a novel, bridge-dependent approach for quantifying the increase of design quantities due to spatially variable earthquake ground motion (SVEGM). Contrary to the existing methods for multiple support bridge excitation analysis that are either too complicated to be applied by most practitioners or oversimplied (e.g. Eurocode 8, Annex D provisions), this method aims to strike a balance between simplicity, accuracy and computational efficiency. The method deliberately avoids generating support-dependent, acceleration or displacement, asynchronous inputs for the prediction of bridge response. The reasons behind this decision are twofold: (a) first, the uncertainty associated with the generation of asynchronous motion scenarios, as well as the exact soil properties, stratification and topography is high while, (b) the response of a bridge is particularly sensitive to the above due to the large number of natural modes involved. It is therefore prohibitive to address SVEGM effects deterministically in the framework of a design code. Instead, this new method is based on two important and well-documented observations: (a) that SVEGM is typically *globally beneficial* but *locally detrimental* [1], and (b) that the local seismic demand increase is very closely correlated with the *excitation of higher modes,* which are not normally activated in the case of uniform ground motion [2,3]. Along these lines, a set of static analyses are specified herein to complement the standard, code-based response spectrum analysis. These static analyses apply spatially distributed lateral forces, whose patterns match the shape of potentially excited anti-symmetric modes. The amplitude of those forces is derived as a function of the expected amplification of these modes according to the process initially proposed by Price et al. [4]. Two real bridges with different structural configurations are used as a test-bed to demonstrate the effectiveness of the new method. Comparison of the results with those obtained through rigorous response history analysis using partially correlated, spatially variable, spectrum-compatible input motions [5] shows that, the simplified method presented herein provides a reasonably accurate estimation of the SVEGM impact on the response of the bridges examined at a highly reduced computational cost. This is essentially an elastic method that is found to be simple, yet precise enough to consist an attractive alternative for the design and assessment of long and/or important bridge structures in earthquake-prone regions.

Keywords: bridges, multiple-support excitation, spatial variability, anti-symmetric modes, seismic codes

1. INTRODUCTION

Bridges are seismically vulnerable components of a transportation network and they can cause severe adverse socioeconomic consequences in case of failure [6]. As they often cross irregular topographic profiles at long distances, they are much more susceptible to the effects of multiple-support excitation in comparison to other structures, such as buildings for instace. The latter relates to the fact that their support points are discrete and they can be separated by several meters apart, hence, seismic motion accross successive piers may vary significantly in terms of arrival time, frequency content and amplitude. This phenomenon introduces a ground motion-related uncertainty that is additional to the standard record-to-record variability particularly for long structures and/or abruptly changing soil profiles [7]. Spatial variability of earthquake ground motion (SVEGM) and its effect on seismic performance of bridges has long been studied [8], while field evidence from previous earthquakes (e.g. Loma Prieta, Kobe) has highlighted its potentially detrimental effects [6,9,10]. Careful processing of data from dense seismographical arrays clearly demonstrates the main sources of asynchronous motion at the base of bridge piers, namely, [11]: (a) the effect of wave passage, that is the finite time required for seismic waves to reach and excite successive support points, (b) loss of coherency (i.e., loss of statistical correlation) of the propagating seismic waves, (c) local site effects, (d) geometrical attenuation of the seismic waves with diastance, and (e) kinematic soil-structure interaction that leads to local (i.e., pier-dependent) filtering of higher frequencies.

It is now common belief that due to SVEGM being strongly case-dependent, deterministic approaches are not adequate to capture the dispersion of structural response attributed to the above phenomena, hence, the problem needs to be studied in a probabilistic manner. Different methods have already been developed for that purpose, each one exhibiting its own shortcomings and limitations. Random vibration analysis (RVA) has been extensively used to quantify the sensitivity of different types of bridges, such as highway [12,13], suspension [14,15] and cable-stayed [14–17] bridges to multi-support excitation. RVA, although consistent with a statistical characterization of the response [18], which is key for performance-based design [19], is unfortunately too complex to be used for most practical purposes. Fundamental principles of random vibration theory have also been exploited as an extension of the response spectrum method for the case of non-synchronous input motion [4,11,18,20–24]. In this context, the Multi-Support Response Spectrum method, introduced by Der Kiureghian & Neuenhofer [11] and extended later by Konakli & Der Kiureghian [18], appears to be the most accurate, with the ground motion characterized by the response spectrum and the response quantities calculated as the mean

of their peak values. A limitation of both RVA and the response spectrum-based methods, however, is that they are inherently solving linear or linearized problems, hence they cannot be easily used for assessing the seismic capacity of existing bridges.

On the other hand, time history analysis (THA) employing partially correlated synthetic accelerograms seems to be a more straightforward option for estimating the structural response in a Monte Carlo framework. In this context, ground motions can be simulated through a variety of existing techniques [25–39], while different approaches have been proposed in the literature to satisfy the seismic codes' requirement for compatibility between the simulated ground motion suites and the target response spectrum [5,26,32,39–43]. Since THA can be used for all degrees and sources of nonlinearity (i.e., both material and geometric), it has been used in several studies for the case of different bridge types [1,3,7,9,10,44–57] at the price of course of computational and post-processing time of the large number of motions that need to be generated, converge to the target coherency and frequency content and be applied at different support points.

An additional dimension of this problem is that despite the extensive research discussed above, currenty, there is no clear trend as per the (beneficial or critical) impact of non-uniform input motion on bridges. If the authors need to make a general statement this would be that SVEGM has an *overall favorable* effect *on average*, which can be also *locally detrimental* as significant response amplifications can also be triggered on specific bridge locations and components (i.e., stoppers, specific piers, cables etc). In fact, the influence of SVEGM on bridge response is a complex problem, depending on the engineering demand parameter (EDP) of interest, its location on the structure, the dynamic characteristics of the bridge in question and the assumptions made regarding the seismic input scenario in terms of ground motion correlation, soil conditions etc. An inherent consequence of this complexity is that it is impossible to deterministically predict response quantities due to asynchronous motion based on scaling [10] or combination [1] of uniform ones.

A second important issue related to the effect of SVEGM is the mechanism associated with the dynamic response of soil-bridge systems under multiple-support excitation. Even though it has been long recognized that the total displacement of a multiply-supported MDOF system is the sum of a pseudo-static and a dynamic component [8], it is the latter that tends to trigger local seismic demand increase due to the excitation of higher anti-symmetric modes. This fact was observed by Harichandran & Wang who employed RVA to study the response of single [58] and two span [59] continuous beams under SVEGM. Zerva [57,58] reached a similar conclusion for the case of N-support continuous beams excited by partially correlated motions, with the second study additionally considering the wave passage effect. Contribution of anti-symmetric modes to

the total response has also been observed for asynchronously excited suspension [14,15,60] and arch [15] bridges. Studies based on THA further revealed the de-amplification of symmetric modes, particularly of the first transverse one in most cases, and the respective amplification of the anti-symmetric ones in the case of straight [1,9,10,47,54,61–63], curved [10,44] and cable-stayed [3,50,64] bridges. Recently, Sextos et al. [3] presented a study for the case of the Evripos cable-stayed bridge using real, free-field and superstructure recordings obtained during the (M_s=5.9, 1999) Athens earthquake providing measured evidence that verified the excitation of higher, primarily antisymmetric, modes of vibration. This observation is also in line with experimental studies conducted for the case of straight [65,66] and curved [67] bridges. In this context, Papadopoulos & Sextos [2] quantified the excitation of anti-symmetric modes and correlated them with bridge response quantities. Common ground in the aforementioned studies is that the amplification and de-amplification of the bridge response quantities is in very good agreement with the excitation of higher anti-symmetric modes and the reduced vibration at the predominant structural modes, respectively.

Despite the aforementioned progress, most seismic codes worldwide do not yet address the SVEGM through a solid approach for the generation and application of spatially variable ground motion suites. Instead, indirect measures, such as larger seating deck lengths and simplified methods are employed. Currently, only two seismic codes (Eurocode 8 – Part 2 for bridges [53] and the New Italian Seismic Code [68]) explicitly deal with the SVEGM; their provisions, aim at capturing solely the increased bridge demand due to the pseudo-static response component, ignoring the excitation impact of higher anti-symmetric modes. In addition, the proedure presented in the current version of Eurocode 8 [53], fails to provide anything but a very minor effect on the predicted design quantities while, by its own static nature, cannot be applied for bridges which are insensitive to statically imposed displacements, such as those designed with seismical isolation [7]. It can thus be concluded that modern seismic codes in the U.S., Europe and Asia do not provide as yet a comprehensive framework for the consideration of SVEGM in the seismic design and assessment of bridges due to the lack of a simple, theoretically sound and code-oriented approach, which will be easily applicable and thus appealing to the civil engineering community.

In this context, the objective of this paper is to present a novel, bridge-dependent, simplified approach for designing bridge structures for multi-support earthquake excitation. The method, which refers to the lateral response of the bridge, aims to offer a different view for solving this complex problem as summarized below:

(a) it does not generate suites of spatially variable earthquake ground motions to predict the structural response, on the grounds that this involves complex simulation procedures and uncertain input that lead to bridge responses that are very sensitive to the assumptions made

(b) it accepts a-priori that: *if* SVEGM effects are significant (e.g. for the case of long bridges or bridges crossing abruptly changing soil profiles), *then* it is only the bridge piers that are associated with the excitation of anti-symmetric higher modes that are detrimentally affected at a local level.

(c) with that in mind it aims to directly quantify the local seismic demand amplification and apply it as an additional safety margin *to critical piers only* without actually running a SVEGM-based THA.

The rational behind this method and the mathematical formulation is presented in the following along with its application for the case of two real bridges for demonstrating its applicability and accuracy against a rigorous asynchronous excitation THA.

2. EQUATIONS OF MOTION & CODE PROVISIONS

2.1 Equations of motion

The assumption of uniform excitation at the support points involving M-degrees of freedom of an N-degrees-of-freedom (N-DOF) system (Fig. 1) is no longer valid in the case of bridge structures of significant length and for those crossing different soil profiles or irregular topographies. Table 1 summarises the differential equation which governs the response of a system under uniform and non-uniform ground motion (Eq.1-8). In these equations **M**, **C**, and **K** are the respective [N×N] mass, damping and stiffness matrices of the N unconstrained DOFs, $\mathbf{M_g}$, $\mathbf{C_g}$, and $\mathbf{K_g}$ are the respective [M×M] mass, damping and stiffness matrices associated with the M-DOF at the supports, $\mathbf{M_c}$, $\mathbf{C_c}$, and $\mathbf{K_c}$ are the respective [N×M] coupling mass, damping and stiffness matrices between the N unconstrained and the M constrained DOF and $\mathbf{u_t}$ and $\mathbf{u_g}$ are the {N×1} and {M×1} vectors of displacements of the unconstrained and the constrained DOF, respectively. In both cases of uniform and non-uniform excitation, the total displacements are decomposed into their dynamic and pseudo-static components (Eq.2). In the first case of uniform motion, **r** is the {N×1} influence vector, which represents the rigid body displacements of the masses related to the active direction of the support motion, while in the second case, **R** is the [N×M] influence matrix, where each column $\{\mathbf{r_k}\}$ represents the static displacements of the unconstrained DOF

when the k[th] support experiences unit displacement while all other supports are fixed. Substituting Eq.2 in Eq.1, considering a lumped mass model ($\mathbf{M_c}$=0) and ignoring the damping terms of the effective force vector in the case of non-uniform excitation as negligible, the equations of motion are significantly simplified (Eq.3). In terms of the latter, the damping term equals zero if the damping matrices are proportional to the stiffness matrix, otherwise it is usually small enough, in relation to the inertia term, to be ignored [69]. In addition, expanding the displacements **u** in terms of modal contribution (Eq.4), with q_i being the modal coordinates, substituting them into Eq.3 and taking advantage of the modes' orthogonality, the N decoupled equations of motion are derived (Eq.5). In these equations Γ_i is the modal participation factor of mode *i* when the structure is uniformly excited and and $\Gamma_{i,k}$ the modal participation factor of the same mode related to the excitation of the k^{th} support under multi-support excitation. It is important to note that, in the case of a structure subjected to uniform input motion, the modal participation factor of mode *i* is defined as: $\Gamma_i = \sum_{k=1}^{M} \Gamma_{i,k}$.

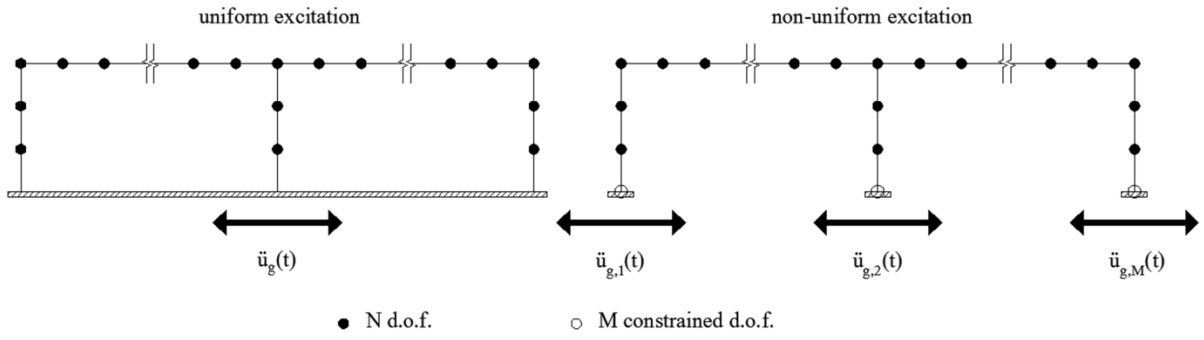

Figure 1. Multi-degree of freedom models under uniform (on the left) and non-uniform (on the right) excitation.

Table 1. Comparative presentation of the equations of motion for uniform & non-uniform excitation.

Uniform excitation	Multi-support excitation	
$\mathbf{M}\ddot{\mathbf{u}}_\mathbf{t} + \mathbf{C}\dot{\mathbf{u}} + \mathbf{K}\mathbf{u} = \mathbf{0}$	$\begin{bmatrix} \mathbf{M} & \mathbf{M_c} \\ \mathbf{M_c^T} & \mathbf{M_g} \end{bmatrix} \begin{Bmatrix} \ddot{\mathbf{u}}_\mathbf{t} \\ \ddot{\mathbf{u}}_\mathbf{g} \end{Bmatrix} + \begin{bmatrix} \mathbf{C} & \mathbf{C_c} \\ \mathbf{C_c^T} & \mathbf{C_g} \end{bmatrix} \begin{Bmatrix} \dot{\mathbf{u}}_\mathbf{t} \\ \dot{\mathbf{u}}_\mathbf{g} \end{Bmatrix} + \begin{bmatrix} \mathbf{K} & \mathbf{K_c} \\ \mathbf{K_c^T} & \mathbf{K_g} \end{bmatrix} \begin{Bmatrix} \mathbf{u}_\mathbf{t} \\ \mathbf{u}_\mathbf{g} \end{Bmatrix} = \begin{Bmatrix} \mathbf{0} \\ \mathbf{P}_\mathbf{g} \end{Bmatrix}$	(1)
$\mathbf{u}_\mathbf{t} = \mathbf{u} + \mathbf{u}_\mathbf{s} = \mathbf{u} + \mathbf{r}u_g$	$\begin{Bmatrix} \mathbf{u}_\mathbf{t} \\ \mathbf{u}_\mathbf{g} \end{Bmatrix} = \begin{Bmatrix} \mathbf{u} \\ \mathbf{0} \end{Bmatrix} + \begin{Bmatrix} \mathbf{u}_\mathbf{s} \\ \mathbf{u}_\mathbf{g} \end{Bmatrix} = \begin{Bmatrix} \mathbf{u} \\ \mathbf{0} \end{Bmatrix} + \begin{Bmatrix} \mathbf{-K^{-1}K_c u_g} \\ \mathbf{u}_\mathbf{g} \end{Bmatrix} = \begin{Bmatrix} \mathbf{u} \\ \mathbf{0} \end{Bmatrix} + \begin{Bmatrix} \mathbf{R u_g} \\ \mathbf{u}_\mathbf{g} \end{Bmatrix}$	(2)
$\mathbf{M}\ddot{\mathbf{u}} + \mathbf{C}\dot{\mathbf{u}} + \mathbf{K}\mathbf{u} = -\mathbf{M}\mathbf{r}\ddot{u}_g$	$\mathbf{M}\ddot{\mathbf{u}} + \mathbf{C}\dot{\mathbf{u}} + \mathbf{K}\mathbf{u} = -\sum_{k=1}^{M} \mathbf{M}\mathbf{r}_k \ddot{u}_{gk}$	(3)
$\mathbf{u} = \mathbf{\Phi}\mathbf{q} = \sum_{i=1}^{N} \boldsymbol{\varphi}_i q_i$	$\mathbf{u} = \mathbf{\Phi}\mathbf{q} = \sum_{i=1}^{N} \boldsymbol{\varphi}_i q_i$	(4)

$\ddot{q}_i + 2\omega_i\zeta_i\dot{q}_i + \omega_i^2 q_i = -\Gamma_i \ddot{u}_g$ $\Gamma_i = \frac{\boldsymbol{\varphi}_i^{\mathrm{T}}\mathbf{M}\mathbf{r}}{\boldsymbol{\varphi}_i^{\mathrm{T}}\mathbf{M}\boldsymbol{\varphi}_i}$	$\ddot{q}_i + 2\omega_i\zeta_i\dot{q}_i + \omega_i^2 q_i = -\sum_{k=1}^{M}\Gamma_{i,k}\ddot{u}_{g,k}$ $\Gamma_{i,k} = \frac{\boldsymbol{\varphi}_i^{\mathrm{T}}\mathbf{M}\{\mathbf{r}_k\}}{\boldsymbol{\varphi}_i^{\mathrm{T}}\mathbf{M}\boldsymbol{\varphi}_i}$	(5)
$q_i = \Gamma_i D_i$	$q_i = \sum_{k=1}^{M} q_{i,k} = \sum_{k=1}^{M}\Gamma_{i,k} D_{i,k}$	(6)
$\mathbf{u} = \boldsymbol{\Phi}\mathbf{q} = \sum_{i=1}^{N}\boldsymbol{\varphi}_i\Gamma_i D_i$	$\mathbf{u} = \boldsymbol{\Phi}\mathbf{q} = \sum_{i=1}^{N}\sum_{k=1}^{M}\boldsymbol{\varphi}_i\Gamma_{i,k} D_{i,k}$	(7)
$\mathbf{u_t} = \mathbf{r}u_g + \sum_{i=1}^{N}\boldsymbol{\varphi}_i\Gamma_i D_i$	$\mathbf{u_t} = \sum_{k=1}^{M}\{\mathbf{r}_k\}u_{g,k} + \sum_{i=1}^{N}\sum_{k=1}^{M}\boldsymbol{\varphi}_i\Gamma_{i,k} D_{i,k}$	(8)
$\mathbf{u}$; $\mathbf{u_t}$; $\mathbf{u_s}$; $\mathbf{u_g}$; $\boldsymbol{u_g}$; $\boldsymbol{u_{g,k}}$; $\boldsymbol{q_i}$; $\boldsymbol{q_{i,k}}$; $\boldsymbol{D_i}$; $\boldsymbol{D_{i,k}}$ and their derivatives are time dependent functions (e.g. u(t))		

Eq.6 is the solution of the i^{th} (i=1,…N), decoupled equation of motion, where $D_i(t)$ is the response of a single DOF oscillator with the dynamic characteristics of mode *i*, subjected to the excitation of the k^{th} support. The dynamic displacements of the system are shown in Eq.7 and the total displacements are given by Eq.8. It can be seen therefore that the dynamic response of an extended structure is considerably different for multi-support and identical input motion excitation. In the first case, the pseudo-static displacements (first term of Eq.8) do not produce any elastic forces as they represent rigid body motion, while the opposite is valid for the respective term under non-uniform motion. However, the difference is not limited to the additional pseudo-static internal forces, but extends to the dynamic component as well, through the different modal participation factors associated with mode *i* and excitation of the k^{th} support DOF. It is worth noting again that the latter, despite its direct impact on the dynamic component of the response, is ignored in the simplified provisions of Eurocode 8 as discussed below.

2.2 EC8 provisions for SVEGM

EC8-Part 2 for bridges [53] provides a simplified framework in its informative Annex D for considering SVEGM in the form of additional pseudo-static internal forces. Two characteristic relative displacement patterns between the supports are considered therein: (a) piers subjected to ground displacements of the same sign but varying amplitude (SET A):

$$d_{ri} = \sqrt{2}d_g\frac{L_i}{L_g} \le \sqrt{2}d_g \tag{9}$$

and (b) successive piers displaced in opposite directions (SET B):

$$d_i = \pm \frac{1}{2} \beta_r \sqrt{2} d_g \frac{L_{av,i}}{L_g} \quad (10)$$

where d_g is the design ground displacement corresponding to the soil type at support i, L_i is the distance from pier i to the reference point (usually the abutment), L_g is the distance beyond which the motion is considered uncorrelated and $L_{av,i}$ is the average distance between $L_{avi,i-1}$ and $L_{avi,i+1}$. The stresses imposed by the above two sets of pseudo-static forces ($E_{i,SetA}$, E_{iSetB}) are derived through static analysis. The maximum action effect arising from the two distinct static cases is then superimposed with the outcome of a typical response spectrum analysis ($E_{i,in}$) by means of the square root of the sum of squares (SRSS) combination rule:

$$E_{sd} = \sqrt{[\max(E_{i,SetA}, E_{i,SetB})]^2 + E_{i,in}^2} \quad (11)$$

Comparative studies on the effectiveness of this simplified approach with more sophisticated ones have highlighted important logical and theoretical issues that may, under certain circumstances, lead to highly unconservative design [7]. In addition, being effectively static in nature, the above force patterns cannot be applied on bridges which are insensitive to statically imposed displacements, such as for instance seismically isolated bridges.

An improved process based on the EC8 provisions was proposed by Sextos & Kappos [7] while a alternative to EC8-Part 2 Annex D procedure was developed by Nuti & Vanzi [13,70]. Recently Falamarz-Sheikhabadi & Zerva [71] introduced a deterministic approach for the derivation of simplified displacement loading patterns that can be used in lieu of those proposed by EC8 and irrespectively of the source-to-site distance. These patterns incorporate the propagation characteristics of seismic waves, i.e. the loss of coherency and the wave passage effect, while also taking into account the contribution of the short period waves on the out-of-phase response of adjacent piers. However, similar to the previous methods, its use is limited to bridges which are sensitive to statically imposed displacements and respond in the linear range.

3. SIMPLIFIED METHOD TO DESIGN BRIDGES ACCOUNTING FOR SVEGM EFFECTS

A novel method is proposed herein to capture the effect of SVEGM. Instead of generating spatially variable acceleration time histories for each bridge support or imposing displacement patterns at the base of each pier, a set of spatially distributed lateral force $\mathbf{F}_i$ (i=1, 2, ...) profiles, whose patterns match the shapes of anti-symmetric modes i (i=1, 2, …), is applied on the structure. The respective set of static analyses is subsequently performed and the responses derived are combined with the

inertial response due to uniform excitation; the latter is calculated through standard methods that are prescribed in the codes, i.e., either by means of the response spectrum or time history analysis. In this context, the lateral force pattern for each mode *i* is proportional to the product of its mode shape φ_i, its circular frequency squared ω_i^2 and the mass assigned to the nodes **M**:

$$\mathbf{F}_i = \left(\overline{SF_i} - 1\right) \cdot \Gamma_i \cdot D_i \cdot \left(\omega_i^2 \mathbf{M} \boldsymbol{\varphi}_\mathbf{i}\right) \tag{12}$$

where Γ_i is the modal participation factor of mode *i*, D_i is the spectral displacement of mode *i* and $\overline{SF_i}$ is a scale factor accounting for the amplified contribution of anti-symmetric mode *i* due to the SVEGM.

In the following, the proposed method is analytically presented and discussed in a stepwise manner; a total set of eleven steps is unfolded. More specifically, **Step 1** defines the earthquake scenario and wave propagation characteristics assumed (power spectum density, coherency model, V_{app}). **Step 2** determines the dynamic properties of the bridge through modal analysis. In **Step 3**, a number of static analyses, equal to the number of supports along the examined direction, is performed and the influence matrix $\mathbf{R}=-\mathbf{K}^{-1}\mathbf{K}_c$ ([NxM]) is constructed. **Step 4** computes the modal participation factors $\Gamma_{i,k}$ (Eq.5b) for each mode *i*. With respect to the examined scenario (Step 1), the non-dimensional spatial variability parameter $\Psi(\omega)$ is calculated in **Step 5**. **Step 6** then estimates the generalized participation factors B_i (i=1,…N) for each mode and their upper bound B_{imax}; the ratios $|B_i(f)|/B_{imax}$, are used to estimate the potentially amplified contribution of anti-symmetric modes due to asynchronous earthquake motion which is key to predict the unfavorable effect of spatial variability on individual Engineering Demand Parameters and design quantities.

These ratios are then compared with the respective ones under uniform excitation $|\Gamma_i|/B_{imax}$ and the frequency-dependent scale factors $SF_i(\omega)$ of response due to asynchronous excitation are derived in **Step 7**. Next, **Step 8** estimates the mean values $\overline{SF_i}$ for each mode across the pre-defined excitation frequency range to get an average value of response amplification. In **Step 9**, a set of static analyses is performed, only for those modes for which $\overline{SF_i} > 1$ (i.e., the effect of spatial variability is detrimental) with loads calculated through Eq.12. Conventional dynamic analysis under uniform excitation is performed in **Step 10**. Finally, **Step 11** combines the response quantities derived from Steps 9 and 10 by means of the SRSS rule. The details of the successive calculation steps are given below.

3.1 Step 1: Ground motion intensity, coherency and propagation velocity

Similarly to all existing methods for multi-support excitation of bridges, a power spectrum density (PSD) and a coherency model need to be defined to characterise the random field of the generated seismic ground motions. In the present method, the sole purpose of the PSD lies in the selection of an excitation frequency range for which the desired (target) level of power is exceeded. To this end, unless a specific PSD corresponding to the region of interest is provided or a method for the conversion of a response spectrum to a PSD is followed, the Clough & Penzien [72] spectrum can readily be used:

$$S(\omega) = S_o \frac{\left(1+4\zeta_g^2\left(\omega/\omega_g\right)^2\right)}{\left(1-\left(\omega/\omega_g\right)^2\right)^2+4\zeta_g^2\left(\omega/\omega_g\right)^2} \frac{\left(\omega/\omega_f\right)^4}{\left(1-\left(\omega/\omega_f\right)^2\right)^2+4\zeta_f^2\left(\omega/\omega_f\right)^2} \tag{13}$$

where S_o is a constant determining the intensity of acceleration at the dedrock level, ω_g and ζ_g are the characteristic frequency and damping ratio of the ground respectively, and ω_f and ζ_f are additional filtering parameters. The Clough & Penzien [72] spectra for soft, firm and medium soil using the parameters reported by Der Kiureghian & Neuenhofer [11] are illustrated in Fig.2. For sites with soil conditions that greatly vary along a bridge, the mean of the individual PSD spectra can be used.

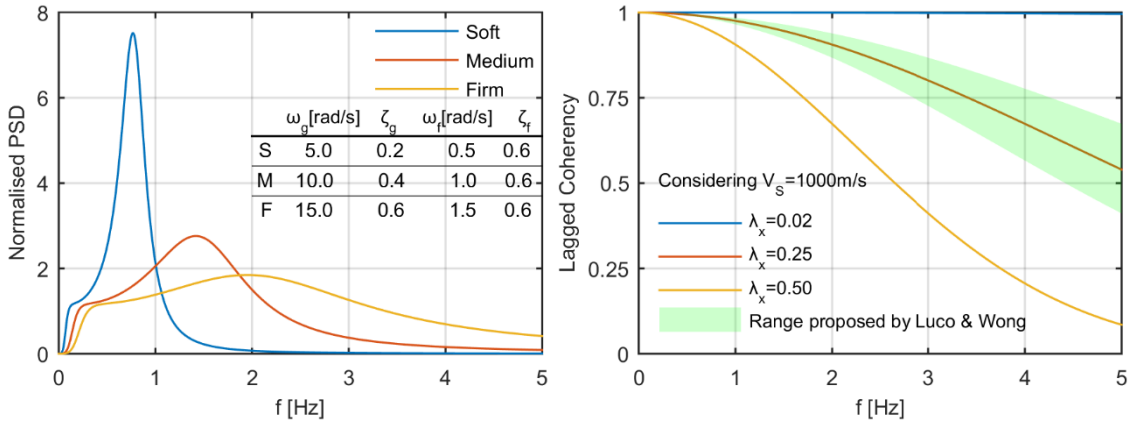

Figure 2. Left: The Clough & Penzien spectra for soft, firm and medium soil using the parameters reported by Der Kiureghian & Neuenhofer (in the embedded table). Right: The Luco & Wong coherency model for different values of λ_x (V_s=1000m/s).

The correlation pattern of the spatially variable generated ground motions also needs to be defined. The semi-empirical formulation proposed by Luco & Wong (1986) [73] can be used as the coherency model:

$$\left|\gamma\left(\xi,\omega\right)\right| = \exp\left[-\left(\lambda_x \omega \xi / V_S\right)^2\right] \quad where \;\; \lambda_x = \mu\left(\mathrm{H}/r_o\right)^{0.5} \tag{14}$$

where μ is a measure of the relative variation of the elastic properties in the medium, H is the distance in the medium traveled by the shear waves, and r_o is the scale length of the random inhomogenities along the path. The ratio of the dimensionless factor λ_x to the shear wave velocity V_S is the drop coherency parameter controling the exponential decay of the function; the higher the ratio the more significant the loss of coherency. According to Luco & Wong [73], a reasonable value for the ratio varies between (2-3)x10^{-4}m^{-1}s, while the dimensionless parameter λ_x typically varies in the range 0.02-0.5 [74]. Fig.2 illustrates the Luco & Wong [73] coherency model for different values of λ_x. The wave passage effect is taken into account through the apparent wave propagation velocity V_{app} which typically varies between 1000-3000m/s (for more information see [8]).

3.2 Step 2: Modal analysis of the bridge

A finite element (FE) model of the bridge is developed as usual. Any structural analysis code can be used as long as the mass **M** ([NxN]) and stiffness matrices **K** ([NxN]) can be exported. A modal analysis follows, in order to determine the natural periods of the bridge T_i, i=1, …, N and its respective modes φ_i ({Nx1}). Matrices **M**, **K** and **Φ** ([NxN]) are then used to calculate the modal participation factors $\Gamma_{i,k}$ (according to eq.15) in Step 4 and the generalized participation factors B_i (eq.25 & eq.26) in Step 5 by means of any mathematical tool (e.g. Matlab [75]).

3.3 Step 3: Influence matrix R (M static analyses)

Having developed the finite element model of the bridge in Step 2, a number of static analyses are performed to construct the influence matrix $\mathbf{R} = -\mathbf{K}^{-1}\mathbf{K_c}$ ([NxM]). The number of analyses required equals the number of bridge supports (= M) along the examined direction. The way this is derived can be easily understood on the basis of matrix **R** interpretation: each column $\{\mathbf{r_k}\}$ of matrix **R** represents the static displacements of the structure's unconstrained DOF when its k^{th} support experiences unit displacement while the rest ones remain fixed.

3.4 Step 4: Modal participation factors $\Gamma_{i,k}$

In this step, the modal participation factors for each mode i (i=1,…N) associated with the k^{th} support excitation (k=1,…M) are calculated as:

$$\Gamma_{i,k} = \frac{\boldsymbol{\varphi}_i^{\mathrm{T}} \mathbf{M} \{\mathbf{r}_k\}}{\boldsymbol{\varphi}_i^{\mathrm{T}} \mathbf{M} \boldsymbol{\varphi}_i} \tag{15}$$

where eigenmodes $\boldsymbol{\varphi}_i$ {Nx1} and mass matrix **M** [NxN] are determined in Step 2, and $\{\mathbf{r}_k\}$ is the k^{th} column of the influence matrix **R** computed in Step 3. Equation $\Gamma_i = \sum_{k=1}^{M} \Gamma_{i,k}$ can be used to verify whether $\Gamma_{i,k}$ has been accurately calculated.

3.5 Step 5: Non-dimensional spatial variability parameter Ψ(ω)

In order to quantify the amplification of the anti-symmetric modes due to SVEGM, a process similar to the one used by Price & Eberhard [4] is followed. Ground motions at the supports **U(ω)** (forming an {Mx1} array) are described in the frequency domain and in relation to the "known" motion at the reference point $U_o(\omega)$, which could be taken at one of the abutments:

$$\mathbf{U}(\boldsymbol{\omega}) = \begin{bmatrix} U_1(\omega) \\ \vdots \\ U_M(\omega) \end{bmatrix} = \boldsymbol{\Psi}(\boldsymbol{\omega}) U_o(\omega) = \begin{bmatrix} \Psi_1(\omega) \\ \vdots \\ \Psi_M(\omega) \end{bmatrix} U_o(\omega) \tag{16}$$

where **Ψ(ω)** ({Mx1} array) is a non-dimensional spatial variability parameter. This non-dimentional parameter effectively expresses the variation of the generated ground motions in the frequency domain with respect to the reference ('known') motion at one of the abutments and is derived according to the following procedure.

Since the Fourier transformation is used for the analysis of the amplitude and the phase of strong ground motion, a sinusoidal wave function can be assumed for each excitation frequency ω_o [71]:

$$u(x,t) = A(\omega_o) \sin(\omega_o t + \omega_o R_\theta x + \varphi_o) \tag{17}$$

where $A(\omega_o)$ is the amplitude that corresponds to the excitation frequency ω_o, which is assumed to remain constant between the piers, x is the distance between each examined support and the reference point, φ_o is the initial phase, and R_θ is given by:

$$R_\theta = \sqrt{\frac{2\lambda_x^2}{V_S^2} + \frac{1}{V_{app}^2}} \tag{18}$$

where λ_x is the dimensionless factor selected in Step 1, controling the exponential decay of the coherency function, V_S is the shear wave velocity in the soil medium, and V_{app} is the apparent wave propagation velocity (reasonable values 1000-3000m/s, but for more information see [8]).

Expressing Eq.17 in the frequency domain, the motion at each pier due to the excitation frequency ω_o is given by:

$$U(x,\omega) = \mathrm{A}(\omega_o)\frac{1}{2}i\left[\delta(\omega+\omega_o)-\delta(\omega+\omega_o)\right]e^{-i\omega\left(-R_\theta x-\frac{\varphi_o}{\omega_o}\right)} = \\ = \mathrm{A}(\omega_o)\frac{1}{2}i\left[\delta(\omega+\omega_o)-\delta(\omega+\omega_o)\right]e^{i\omega R_\theta x+i\frac{\omega\varphi_o}{\omega_o}} \tag{19}$$

which, in the case of the reference point, takes the form:

$$U(x=0,\omega) = \mathrm{A}(\omega_o)\frac{1}{2}i\left[\delta(\omega+\omega_o)-\delta(\omega+\omega_o)\right]e^{i\frac{\omega\varphi_o}{\omega_o}} \tag{20}$$

Substituting Eq.19 and Eq.20 into Eq.16, each element $\Psi_x(\omega)$ (x=1,…,M) of $\mathbf{\Psi(\omega)}$ results in:

$$\Psi_x(\omega) = \frac{U(\omega)}{U_o(\omega)} = \frac{e^{i\omega R_\theta x+i\frac{\omega\varphi_o}{\omega_o}}}{e^{i\frac{\omega\varphi_o}{\omega_o}}} = e^{i\omega R_\theta x} = e^{i\omega\sqrt{\frac{2\lambda_x^2}{V_S^2}+\frac{1}{V_{app}^2}}x} \tag{21}$$

In the above equation, the non-dimensional spatial variability parameter $\Psi_x(\omega)$ depends on the assumed ground motion model of Step 1. In this context, calculation of $\Psi_x(\omega)$ is made as follows:

(a) In the conventional case of fully coherent ground motions along the bridge supports where wave passage is ingored (i.e., uniform excitation), $\lambda_x=0$, $V_{app}\rightarrow\infty$ hence, $\Psi_x(\omega)=1$.

(b) In the idealized case where wave passage effect is indeed accounted for but ground motions are fully correlated, the waveform travels with finite apparent propagation velocity V_{app}, the coherency drop parameter is $\lambda_x=0$ and $\Psi_x(\omega)$ is defined as:

$$\Psi_x(\omega) = \exp\left(i\frac{\omega}{V_{app}}x\right) \tag{22}$$

(c) In the case that both wave passage and incoherency are accounted for, $\Psi_x(\omega)$ depends on the assumed values of λ_x and V_{app} according to Eq. 21.

3.6 Step 6: Generalized participation factor B_i: identification of the excited modes

For each mode i, (i=1,…,N), substituting Eq.16 in the decoupled Eq.5 (expressing the latter in the frequency domain and with mode i normalized so that $\mathrm{M}_i = \boldsymbol{\varphi}_i^{\mathrm{T}}\mathbf{M}\boldsymbol{\varphi}_i$ equals unity) results in:

$$\ddot{Q}_i(\omega) + 2\omega_i\zeta_i\dot{Q}_i(\omega) + \omega_i^2 Q_i(\omega) = \left(\boldsymbol{\varphi}_i^{\mathrm{T}}\mathbf{M}\mathbf{R}\right)\left(-\omega^2\boldsymbol{\Psi}(\boldsymbol{\omega})U_o(\omega)e^{-i\omega t}\right) \tag{23}$$

where $Q_i(\omega)$ is the Fourier component of q_i. A harmonic solution for Q_i is obtained by solving the following equation:

$$Q_i = \mathrm{A}_i\mathrm{B}_i U_o(\omega)e^{-i\omega t} \tag{24}$$

where A_i is the dynamic amplification factor, and B_i is the generalized participation factor defined as:

$$\mathrm{B}_i(\omega) = \left(\boldsymbol{\varphi}_i^{\mathrm{T}}\mathbf{M}\mathbf{R}\right)\boldsymbol{\Psi}(\boldsymbol{\omega}) \tag{25}$$

Note that $B_i(\omega)$ is a frequency dependent complex number for the case of non-uniform excitation, or takes the value of the conventional modal participation factor Γ_i for the uniform excitation case.

Since B_i does not depend on the properties of the "actual" support time histories but on the model used to represent the spatial variability of ground motion, the ratio:

$$\frac{\left|\mathrm{B}_{\mathrm{i}}(\omega)\right|}{\mathrm{B}_{\mathrm{i,max}}} = \frac{\left|\mathrm{B}_{\mathrm{i}}(\omega)\right|}{\sum_{k=1}^{M}\left|\left(\boldsymbol{\varphi}_{\mathbf{i}}^{\mathrm{T}}\mathbf{M}\mathbf{K}^{-1}\mathbf{K}_{\mathbf{c}}\right)_k\right|} \tag{26}$$

can be used to quantify the potentially amplified contribution of the excited anti-symmetric modes. This ratio was first defined by Price & Eberhard [4] who used it in the framework of a coherent analysis in order to modify the modal participation factors of the anti-symmetric modes. In their approach, the frequency dependence of $\mathrm{B_i}$ was ignored and it was only evaluated each time at the natural frequency of the examined mode. In Eq.26, $B_{i,max}$ is the upper bound of B_i, which is different from the absolute value of modal participation factor Γ_i used under synchronous input motion:

$$\left|\Gamma_i\right| = \left|\sum_{k=1}^{M}\left(\boldsymbol{\varphi}_{\mathbf{i}}^{\mathrm{T}}\mathbf{M}\mathbf{K}^{-1}\mathbf{K}_{\mathbf{c}}\right)_k\right| \neq \mathrm{B}_{i,\max} = \sum_{k=1}^{M}\left|\left(\boldsymbol{\varphi}_{\mathbf{i}}^{\mathrm{T}}\mathbf{M}\mathbf{K}^{-1}\mathbf{K}_{\mathbf{c}}\right)_k\right| \tag{27}$$

In the framework of the present simplified method, the ratio $|B_i(f)|/B_{imax}$ is calculated for each mode *i* (either symmetric or anti-symmetric) in a desired range of excitation frequencies (e.g. 0.2-20Hz). Fig.3 illustrates indicative shapes of this ratio for the case of a symmetric (Fig.3 top) and an anti-symmetric mode (Fig.3 bottom) and for different earthquake scenarios: (a) considering only the wave passage effect (Fig.3 left), (b) considering both the wave passage effect and the loss of coherency (Fig.3 middle), and (c) considering a perfectly uniform motion ($V_{app}\rightarrow\infty$) (Fig.3 right). These results correspond to the case of the Lissos bridge, which is subsequently presented in Section 4 (with the symmetric and anti-symmetric modes corresponding to the 3rd and 4th ones cf. Fig.8).

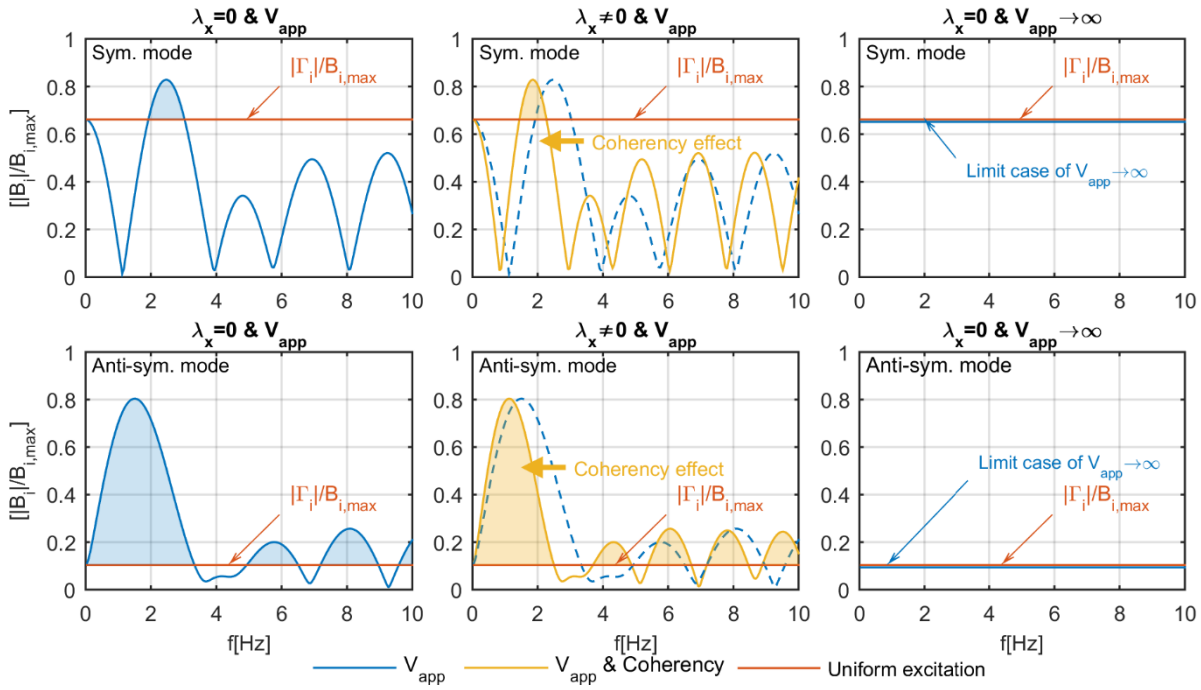

Figure 3. Indicative shapes of the $|B_i(f)|/B_{i,max}$ ratio in the case of symmetric (top) and anti-symmetric (bottom) modes for three different earthquake scenarios. The results refer to Lissos bridge (Section 4).

From Fig.3 it can be seen that spatial variability of earthquake ground motion significantly amplifies the contribution of the anti-symmetric modes (highlighted regions in Fig.3 bottom) in the total structural response and almost throughout the whole excitation frequency range, when compared to the uniform excitation (red line). On the other hand, except for some narrow frequency ranges that may arise (highlighted areas in Fig.3 top), it generally de-amplifies the contribution of the symmetric ones. Comparing the left and middle parts of Fig.3 it can also be observed that, when the loss of coherency is additionally taken into account, the $|B_i(f)|/B_{imax}$ curve, despite retaining its shape, is shifted towards lower frequencies. It is important to note that, as anticipated, the $|B_i(f)|/B_{imax}$ ratio matches the boundary $|\Gamma_i|/B_{imax}$ ratio as the excitation frequency tends to zero

(Fig.3 left & middle) or as the V_{app} tends to infinity while λ_x=0 (Fig.3 right). With respect to the latter case of synchronous excitation, it could be expected that the ratio $|B_i(f)|/B_{imax}$ would be equal to zero given that, as it is well-known, anti-symmetric modes have no contribution to the response under synchronous ground motion. However, this would only be valid in the case of fully symmetric structures, something rarely met in real bridges. Since the results presented herein refer to the non-symmetrical Lissos bridge (Section 4), the terms "symmetric" and "anti-symmetric" are used in a wider scense. This is also illustrated in the modal participation factors of these modes when considering uniform excitation; these are equal to Γ_3=-8.67≠0 for the anti-symmetric and Γ_4=34.45≠0 for the "symmetric" mode. As such, the respective $|B_i(f)|/B_{imax}$ ratios are calculated as 0.103 and 0.662 (cf. Table 2 of Section 4.4).

3.7 Step 7: Frequency-dependent scale factor $SF_i(\omega)$: quantification of the excited modes

Based on the results of Step 6, the scale factor (i.e., degree of amplification/deamplification) $SF_i(\omega)$ for the modal participation factor of mode *i* due to multi-support excitation is given by the ratio:

$$SF_i(\omega) = \frac{\left|B_i(\omega)\right| / B_{i,\max}}{\left|\Gamma_i\right| / B_{i,\max}} \tag{28}$$

Fig.4 presents an example corresponding to the anti-symmetric mode of Fig.3 (bottom) (Step 6): $SF_i(\omega)$ (or $SF_i(f)$ as presented in figures) represents the ratio of the blue (wave passage effect) or yellow (wave passage effect & coherency) curves over the, straight, frequency-independent red lines of uniform excitation shown in Fig.3. It can be observed that, in the case of asynchronous ground motion, the scale factor corresponding to the anti-symmetric mode exceeds unity, having peaks at specific frequencies (see section 5.3), while, as anticipated, under uniform excitation the scale factor is $SF_i(f)$=1 (Fig.4 right). This is effectively the key proxy used herein for higher mode excitation due to SVEGM.

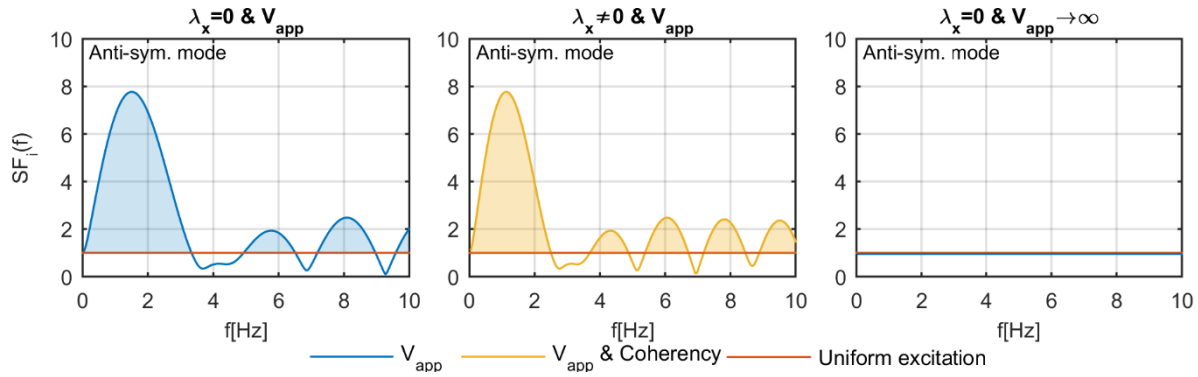

Figure 4. Indicative shapes of the frequency dependent scale factor $SF_i(f)$ in the case of anti-symmetric mode for three different earthquake scenarios (cf. Fig.3 bottom). The results refer to Lissos bridge (Section 4).

3.8 Step 8: Mean scaling factor $\overline{SF_i}$ across the frequency range of interest

Due to the fact that $SF_i(\omega)$ (or $SF_i(f)$ as presented in figures) is frequency-dependent, the need arises to define a mean value $\overline{SF_i}$ that can be easily used for design purposes. As a result, a specific frequency bandwidth needs to be defined. A reasonable assumption is to adopt the frequency range that exceeds a certain level of the assumed PSD, similar to the one used in the case when partially correlated motions are generated in a time history analysis framework. Herein, the bandwidth is proposed to be measured at the level where the power of the spectrum equals $\left(1/\sqrt{2}\right) PSD_{\max}$, based on the definition of the respective bandwidth on the Fourier spectra of an accelerogram [76]. Fig.5 provides an illustrative example of the bandwidth definition in the case of the Clough & Penzien PSD for firm, medium and soft soil conditions. Any other PSD (including an evolutionary one) could be used instead. Estimation of the $\overline{SF_i}$ in the desired range is performed for each mode *i*, {i=1,…N} but to be practical, only modes exhibiting $\overline{SF_i}$ >1 (i.e., detrimental amplification due to SVEGM) are picked to be exploited in Step 9.

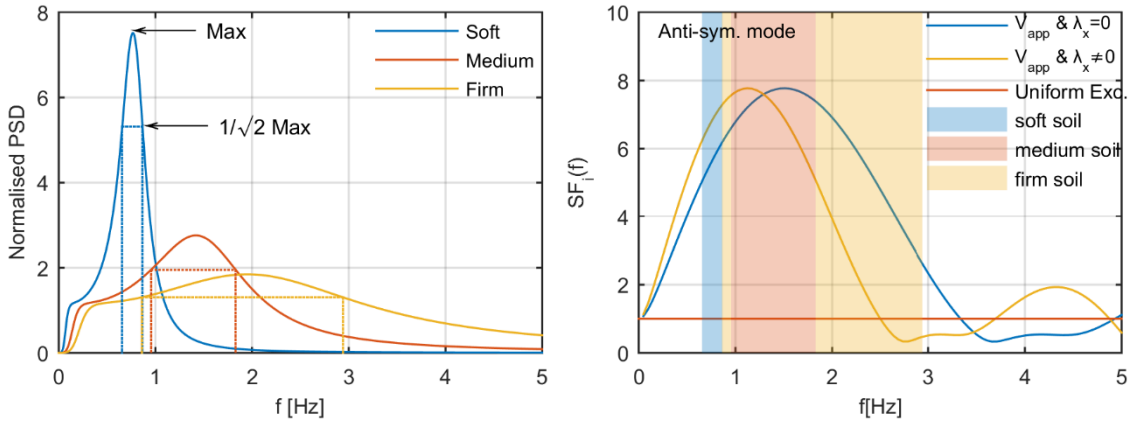

Figure 5. Definition of the bandwidth in which the mean mode amplification scale factor $\overline{SF_i}$ is estimated for the case of the Clough & Penzien PSD and for (a) firm: 0.86-2.94Hz, (b) medium: 0.955-1.83Hz, and (c) soft: 0.655-0.865Hz soil (Der Kiureghian & Neuenhofer [11] parameters used for the spectra).

3.9 Step 9: Static analyses with lateral force patterns F_i

Having identified (Step 6) and quantified (Steps 7-8) the higher modes that have can be excited by spatially variable ground motions, a set of elastic static analyses is performed, for all modes with $\overline{SF_i} > 1$ with loads calculated by the following expression:

$$\mathbf{F}_i = \left(\overline{SF_i} - 1\right) \cdot \Gamma_i \cdot D_i \cdot \left(\omega_i^2 \mathbf{M}\boldsymbol{\varphi}_\mathbf{i}\right) \tag{29}$$

In Step 11, the response quantities derived from these static analyses (which take into account the additional stresses imposed by the spatial variability of earthquake ground motion) are combined with the respective ones obtained through conventional analysis under the assumption of uniform ground motion (Step 10). In Eq. 29, the subtracted "-1" term essentially restricts the contribution of these forces to be accounted only once in the total uniform response of Step 10.

3.10 Step 10: Conventional analysis for uniform ground motion

Any of the available methods for the dynamic analysis of bridges (e.g. response spectrum or linear time history analysis) can be used to derive the uniform-excitation design quantities according to the applied seismic code provisions. Special attention should be paid, though, for the case of time history analysis; the peak response extracted should be used in Step 11.

3.11 Step 11: Bridge design quantities considering SVEGM effects

In this step, the response quantities derived from the conventional analysis of Step 10 ($M_{conv.}$) are combined with the respective quantities (M_{Fi}) under asynchronous excitation estimated in Step 9 by applying the SRSS rule:

$$M = \sqrt{M_{conv.}^2 + \sum_i M_{F_i}^2} \quad (30)$$

Overall, the method introduced herein focuses on the dynamic properties of the bridge as a proxy of its potential amplification due to spatial variability. Currently, the assumption is made that the soil is uniform, however, the mean soil properties can be employed when defining the PSD for the case that ground conditions significantly vary along the bridge length. Since the method is based on the natural modes of a bridge, it is essentially an elastic method. In the following, the accuracy of the proposed method is verified for the case of two real bridges, against the predictions of rigorous time history analysis using partially correlated seismic ground motions.

4. APPLICATION

4.1 Overview

Two real bridges in Greece were used as a test-bed to study the applicability and efficiency of the proposed method for considering the impact of asynchronous excitation on the seismic response of bridges. Uniform soil conditions of soil type A (EC8), maximum ground acceleration a_g of 0.16g and collectively, three seismic input motion scenarios were assumed: (a) synchronous excitation, (b) asynchronous excitation due to finite wave propagation velocity V_{app}=1000m/s, and (c) asynchronous excitation due to partially correlated input motion with V_{app}=1000m/s and λ_x=0.5 (dimensionless drop coherency parameter). It must be noted that values of V_{app} and λ_x in cases (b) and (c) are indicative and can be substituted with any other value within their valid range. The effects of multi-support excitation were summarized through the impact mean ratios 'ϱ', defined as the maximum seismic demand at each pier (e.g. pier base bending moments) under asynchronous ground motion, over the respective EDP under uniform input motion.

4.2 Bridge description

4.2.1 Lissos bridge

The Lissos River motorway bridge is an 11-span, base-isolated, R/C structure with an overall length of 433m, located along the Egnatia Highway in northeastern Greece [77]. It consists of two independent branches. The deck is a continuous, single-cell, pre-stressed concrete box with a constant depth of 2.75m and 14.25m wide (concrete class B35 (kg/cm^2), reinforcing steel class St420/500, pre-stressing steel class St1570/1770), resting through elastomeric bearings on 10 piers and roller bearings (450x600x55.5, with movement capacity +265mm/-365mm) on the abutments. The expansion joints are 330mm.

The transverse displacement of the deck over each pier is restricted to 10cm by stoppers of 1.20m height, while it is prevented at the abutments through lateral elastomeric bearings. The piers are made of reinforced concrete (class B35, reinforcing steel class St420/500) and their heights vary between 4.50m to 10.50m. Fig. 6 illustrates the cross sections of the piers and the deck. This particular bridge was adopted for study on the following grounds: (a) it is long enough for being sensitive to to spatial variability, (b) it has been extensively studied for both synchronous and asynchronous ground motion scenarios, and (c) it is insensitive to statically imposed displacements which are applied in the framework of the simplified Eurocode 8 methods.

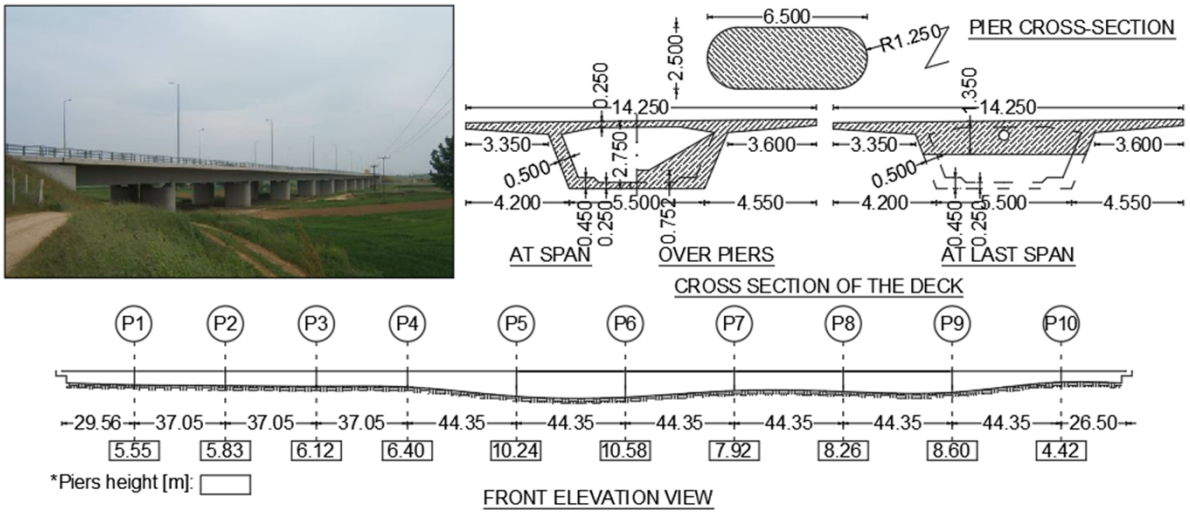

Figure 6: The Lissos River road bridge and its cross sections (dimensions units: meters).

4.2.2 Metsovo bridge

The ravine bridge of Metsovo (Fig. 7) is a 4-span R/C structure, consisting of two independent branches with an overall length of 537m, located along the Egnatia Highway in northwestern Greece. Holding the record of the tallest bridge of the Egnatia motorway (the tallest pier being 110m high), it was constructed with the balanced cantilever method. The deck is a continuous, single-cell, limited pre-stressed concrete box, with a varying depth from 13.0m (at pier M2) to 4.0m (in the key section) (concrete class B45) and a width of 13.95m. The superstructure is monolithically connected to piers P2 (110m high) and P3 (35m high) (concrete class B45), resting through pot bearings on pier P1 (45m high) (concrete class B45) and roller bearings on the abutments. Piers P2 and P3 are founded on large circular Ø12m rock sockets in the steep slopes of the Metsovitikos river ravine, at depths of 25m and 15m respectively. Fig.7 illustrates the cross sections of the piers and the deck. In constrast to the Lissos bridge, this one was selected due to its monolithical connection at the two pies.

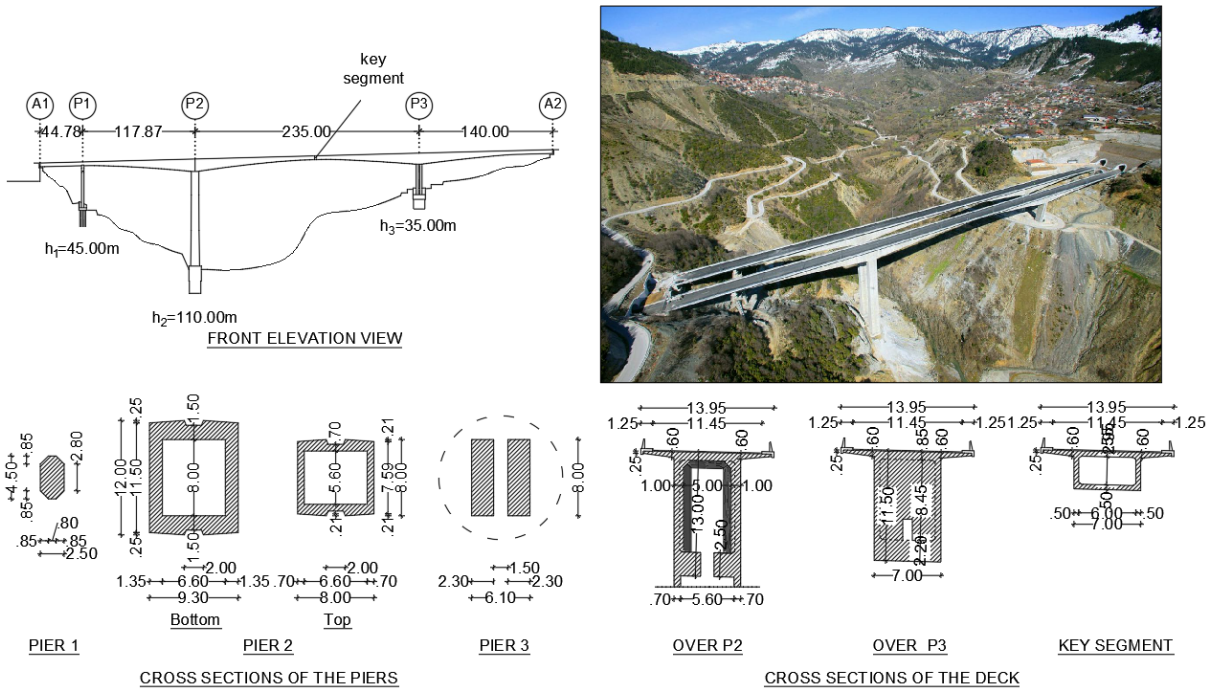

Figure 7: The ravine Metsovo bridge and its cross sections (dimensions units: meters).

4.3 Numerical analysis

Finite element models of both bridges were developed in SAP2000 [78]. In these, the piers, the deck and the stoppers were simulated with beam elements while the elastomeric bearings of the Lissos bridge (equivalent linear properties at secant stiffness assumed) and the pot bearings of the Metsovo bridge were modeled with link elements. Link elements were also used to simulate the gaps between the deck and the stoppers; however, since the proposed approach is restricted to linear response analysis, gaps were considered to be inactive (gap opening assumed to be infinite) in order for geometrical non-linearities due to pounding to be excluded during the validation process (THA). The base of the piers was considered fixed and the deck at the abutments was assumed pinned along the transverse, and free to slide along the longitudinal direction. Fig.8 and 9 illustrate the eigenmodes with participating mass ratios greater than 1% along the transverse direction U_y or around the vertical axis R_z for the Lissos and the Metsovo bridge, respectively. Conventional analysis under uniform ground motion (as required in Step 10 of the proposed methodology) was performed by means of the response spectrum analysis using the design response spectrum (Type 1) of EC8 assuming a behavior factor q=1. This spectrum was also used as the target one for the generation of partially correlated motion sets used in the validation process (Section 5). In the latter case, multi-support excitation was applied to the bridge in the form of displacement time histories; these were calculated from the respective synthetic accelerograms after

being subjected to the necessary baseline correction with the use of the appropriate, for each case, second order polynomial. The Newmark's method for direct integration (γ=1/2, β=1/4) was employed to solve the motions' differential equations, while energy dissipation was modeled through Rayleigh damping.

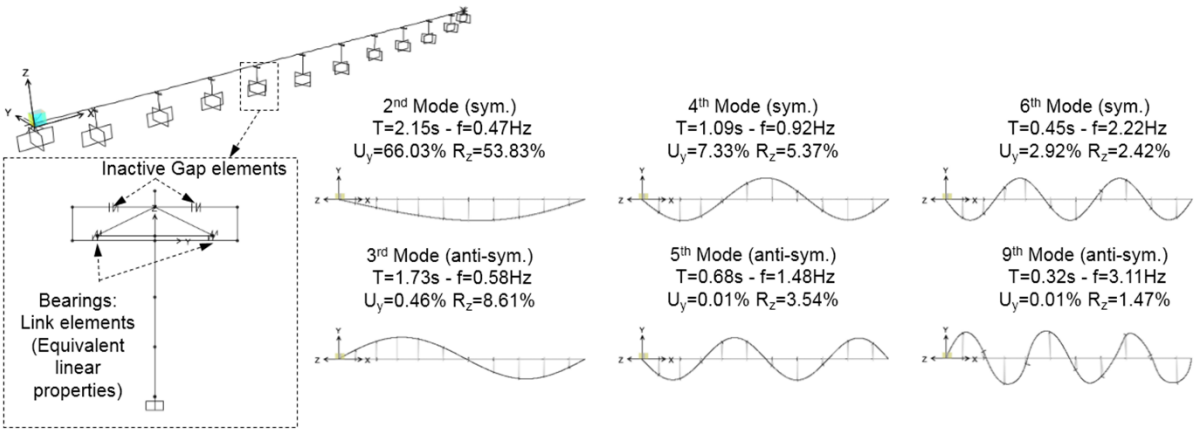

Figure 8: Finite element model of the Lissos bridge and its eigenmodes with participating mass ratios greater than 1% along the transverse direction U_y or around the vertical axis R_z.

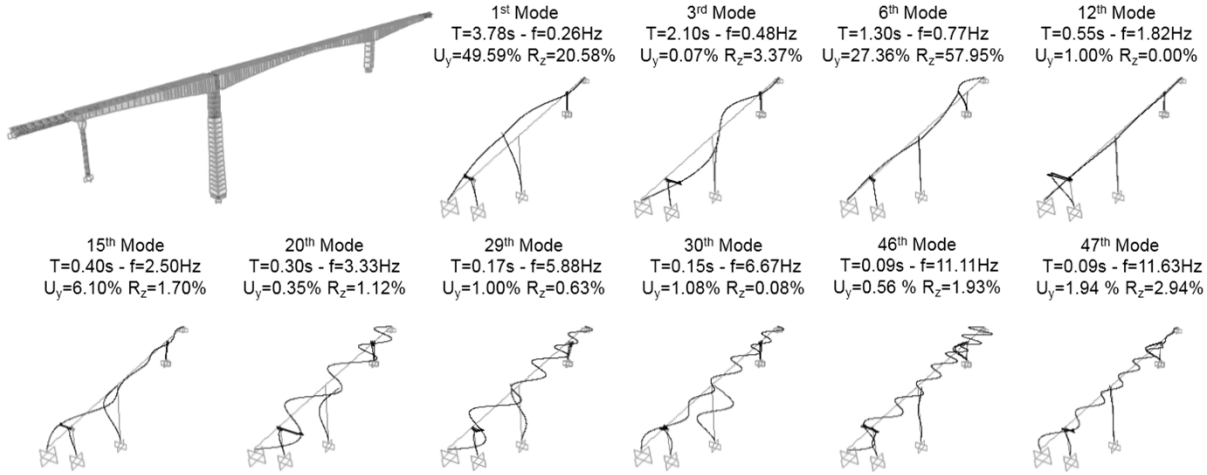

Figure 9: Finite element model of the Metsovo bridge and its eigenmodes with participating mass ratios greater than 1% along the transverse direction U_y or around the vertical axis R_z.

4.4 Application of the proposed method for Lissos and Metsovo bridges

Application of the proposed method for the two bridges was made following the 11 steps outlined in Section 3. After obtaining the [NxN] mass **M** and stiffness **K** matrices, modal analysis was employed to determine the structures' eigenperiods and eigenmodes, with those with participating mass ratios greater than 1% along the transverse direction U_y or around the vertical axis R_z illustrated in Fig.8 and Fig.9 for the Lissos and Metsovo bridges respectively. Considering only transverse excitation, the [NxM] influence matrices **R** were computed. Since the k^{th} column $\{\mathbf{r_k}\}$

of the influence matrix **R** corresponds to the structure's response under unit static displacement at the k^{th} support DOF (with all other support DOFs constratined), twelve static analyses for the Lissos and five static analyses for the Metsovo bridge were performed. Modal participation factors for each mode i associated with the k^{th} support excitation were calculated by Eq. 15. The values of $\Gamma_{i,k}$ illustrated in Fig. 8 and 9 are respectively summarized in Tables 2 and 3. In these tables, the last column is dedicated to the conventional modal participation factors Γ_i. These are computed directly by SAP2000 [78] and are used to verify the accuracy of the $\Gamma_{i,k}$ computation according to $\Gamma_i = \sum_{k=1}^{M} \Gamma_{i,k}$.

Table 2: Modal participation factors $\Gamma_{i,k}$ of the eigenmodes of Lissos bridge with participating mass ratios greater than 1% along the transverse direction U_y or around the vertical axis R_z.

Mode	$\Gamma_{i,1}$	$\Gamma_{i,2}$	$\Gamma_{i,3}$	$\Gamma_{i,4}$	$\Gamma_{i,5}$	$\Gamma_{i,6}$	$\Gamma_{i,7}$	$\Gamma_{i,8}$	$\Gamma_{i,9}$	$\Gamma_{i,10}$	$\Gamma_{i,11}$	$\Gamma_{i,12}$	Γ_i
2	1.3	2.1	5.1	8.5	12.3	14.8	16.1	15.8	12.2	7.7	2.8	4.8	103.4
3	-10.1	-3.3	-7.1	-9.7	-10.1	-5.8	0.5	6.5	8.7	7.0	2.9	11.8	-8.67
4	13.3	1.8	3.3	2.9	0.4	-3.2	-4.1	-1.6	2.0	3.3	1.7	14.5	34.45
5	11.7	0.9	1.2	0.2	-1.3	-1.3	0.5	1.6	0.4	-1.1	-0.9	-13.2	-1.20
6	9.9	0.5	0.4	-0.4	-0.7	0.3	0.7	-0.3	-0.6	0.2	0.5	11.3	21.75
9	-7.9	-0.2	-0.1	0.3	0.1	-0.3	0.2	0.2	-0.3	0.0	0.2	8.9	0.97

Table 3: Modal participation factors $\Gamma_{i,k}$ of the eigenmodes of Metsovo bridge with participating mass ratios greater than 1% along the transverse direction U_y or around the vertical axis R_z.

Mode	$\Gamma_{i,1}$	$\Gamma_{i,2}$	$\Gamma_{i,3}$	$\Gamma_{i,4}$	$\Gamma_{i,5}$	Γ_i
1	-15.83	-0.41	-97.66	-47.65	13.64	-147.90
3	26.21	0.29	16.21	-47.99	10.63	5.36
6	-3.54	-0.06	2.55	-87.83	-20.99	-109.87
12	-0.60	-26.10	6.75	-2.67	1.97	-20.66
15	-8.57	-1.77	-39.64	1.61	-3.51	-51.89
20	7.52	-0.60	-10.38	-1.35	-7.69	-12.50
29	5.94	-0.32	8.11	1.87	5.07	20.68
30	-2.50	0.67	-24.07	-0.13	4.21	-21.82
46	2.95	-0.39	1.54	-14.51	-5.25	-15.67
47	-3.16	0.38	-1.24	-24.47	-0.75	-29.25

As already explained, three ground motion scenarios were defined: (a) synchronous excitation, (b) asynchronous excitation due to finite wave propagation velocity V_{app}=1000m/s, and (c) asynchronous excitation due to fully-asynchronous input motion with V_{app}=1000m/s and λ_x=0.5. The non-dimensional spatial variability parameter $\Psi(\omega)$ and the generalized participation factor $B_i(\omega)$ for each mode i were calculated using Eq.21 and Eq.25 in all three cases, for a range of excitation frequencies between 0-20Hz.

For the effect of SVEGM on bridge response to be quantified, the ratios $|B_i(f)|/B_{imax}$ were computed, with Fig. 10 and Fig. 11 depicting them for the case of Lissos bridge under asynchronous ground motion scenarios (b) and (c) respectively. The frequency-independent ratios $|\Gamma_i|/B_{imax}$, corresponding to uniform ground motion scenario (a), are also shown in the same

figures with a dashed line type. From the above figures, it can be concluded that the SVEGM significantly amplifies the contribution of the anti-symmetric modes (right part of the figures) to the total structural response almost throughout the whole excitation frequency range, while, except for some narrow frequency ranges, generally de-amplifies the contribution of the symmetric ones. Comparing Fig.10 with Fig.11 it can observed that, when the loss of coherency is additionally taken into account, the $|B_i(f)|/B_{imax}$ curve, despite retaining its shape, makes a shift towards lower frequencies. In addition, as already discussed and is anticipated, the $|B_i(f)|/B_{imax}$ ratio matches the boundary $|\Gamma_i|/B_{imax}$ one as the excitation frequency tends to zero or as the V_{app} tends to infinity while $\lambda_x=0$ (Fig.12).

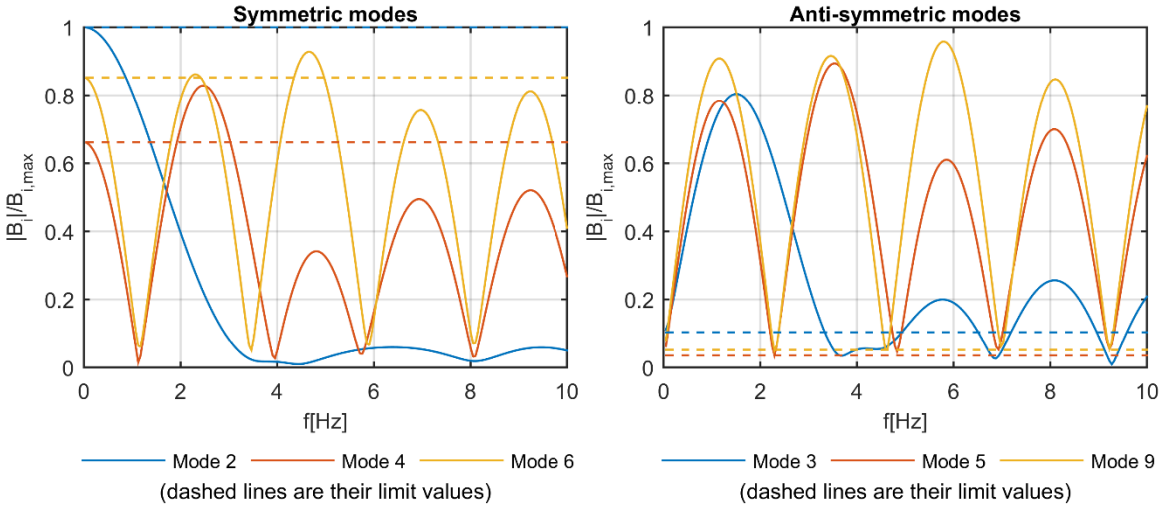

Figure 10: $|B_i(f)|/B_{imax}$ ratios of the modes for the Lissos bridge considering the wave passage effect (V_{app}=1000m/s and λ_x=0).

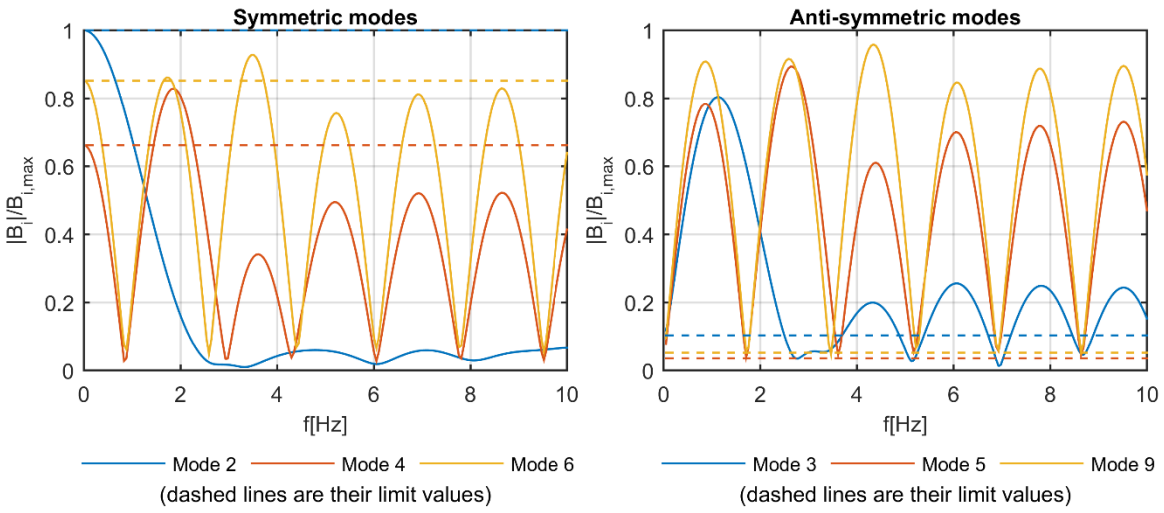

Figure 11: $|B_i(f)|/B_{imax}$ ratios of the modes for the Lissos bridge considering both the wave passage effect and the loss of coherency (V_{app}=1000m/s and λ_x=0.50).

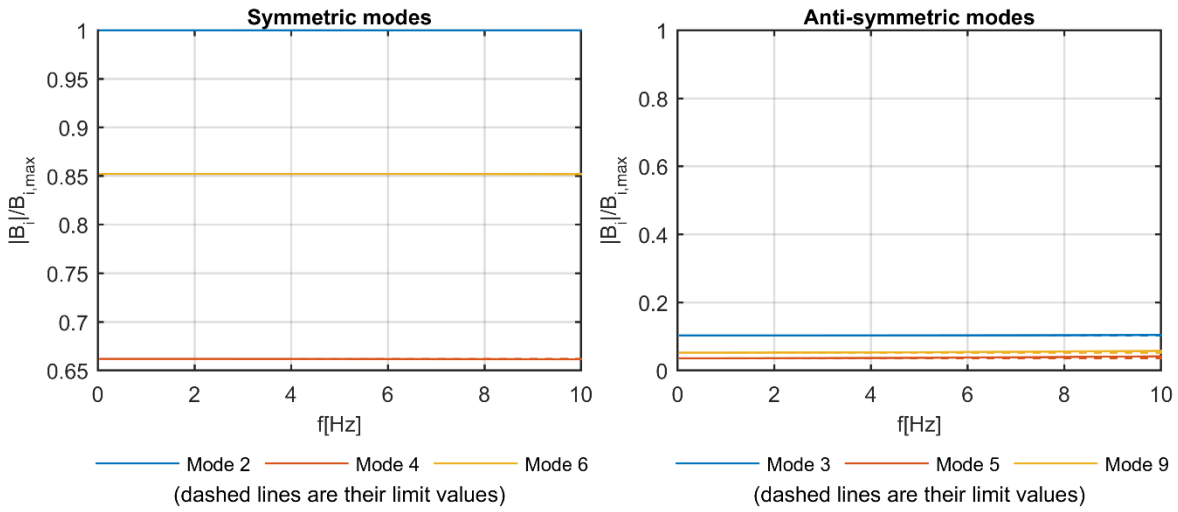

Figure 12: $|B_i(f)|/B_{imax}$ ratio of the symmetric and anti-symmetric modes for the Lissos bridge considering V_{app}=500000m/s (time delay from Ab1 to Ab2 = 0.0009sec) and λ_x=0.

Scale factors $SF_i(\omega)$ (or $SF_i(f)$ as presented in figures) for each modal participation factor of mode i were then computed (Eq.28). Despite V_{app} being equal to 1000m/s in the analyses, $SF_i(\omega)$ were additionally calculated in the V_{app} range between 100-2000m/s. This would not be needed in an actual design case, but is presented herein to facilitate better understanding of the key problem parameters.

The higher mode scale factor $SF_i(\omega)$ for the Lissos bridge under ground motion scenarios (b) and (c) are respectively presented in Fig. 13 and Fig. 14 with cross sections of the surface graphs illustrated in Fig. 15 and Fig. 16. In Fig. 13 and Fig. 14, the V_{app}=1000m/s case is indicated with a black line, while in Fig. 15 and Fig. 16, each colored line corresponds to a specific mode with the red bullets pointing to the excitation frequency that matches the mode's natural frequency. As can be seen, apart from the excitation frequency coinciding with its natural one (red bullet), there exist several other frequencies that may amplify the contribution of a specific mode. Moreover, since $SF_i(\omega)$ (or $SF_i(f)$ as presented in figures) is frequency dependent, its mean value $\overline{SF_i}$ in a specific bandwidth was also estimated. This bandwidth (highlighted in green in Fig.15 and 16) corresponds to the frequency range 1.273-3.66Hz which exceeds the $\left(1/\sqrt{2}\right)PSD_{\max}$ level of the assumed Clough & Penzien evolutionary PSD used in the validation process of Section 5, where partially correlated motions were generated under the time history analysis framework.

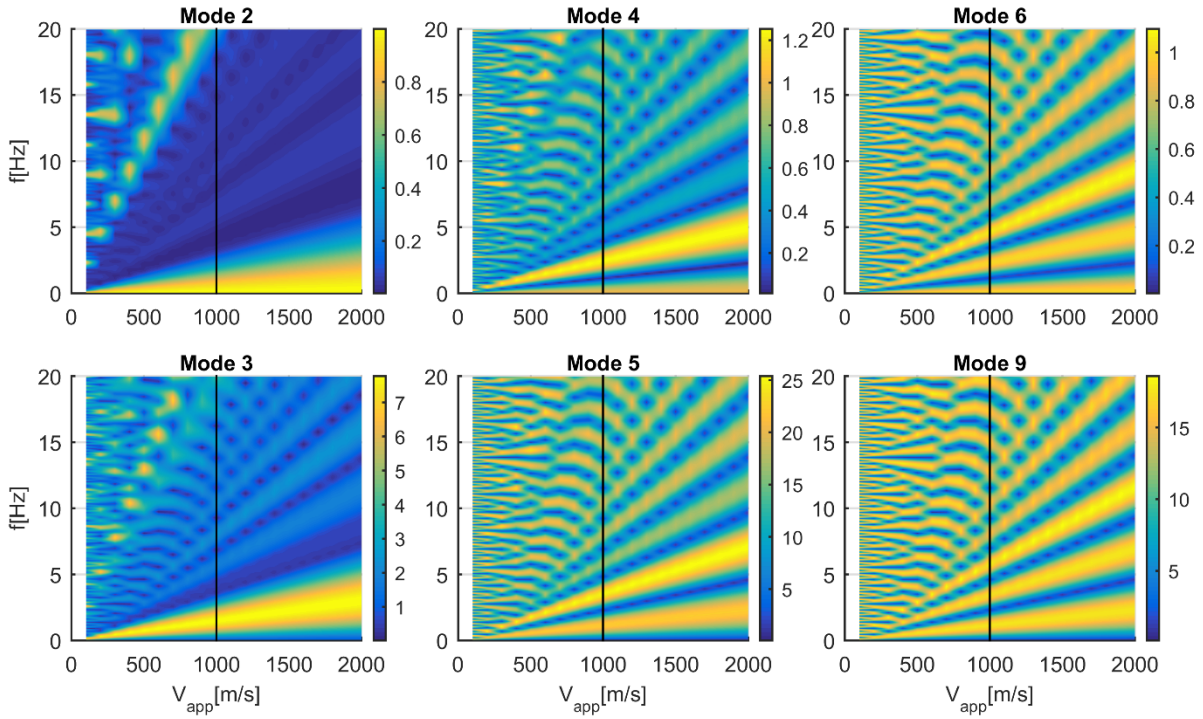

Figure 13: Scale factors $SF_i(\omega)$ for the Lissos bridge under the wave passage effect.

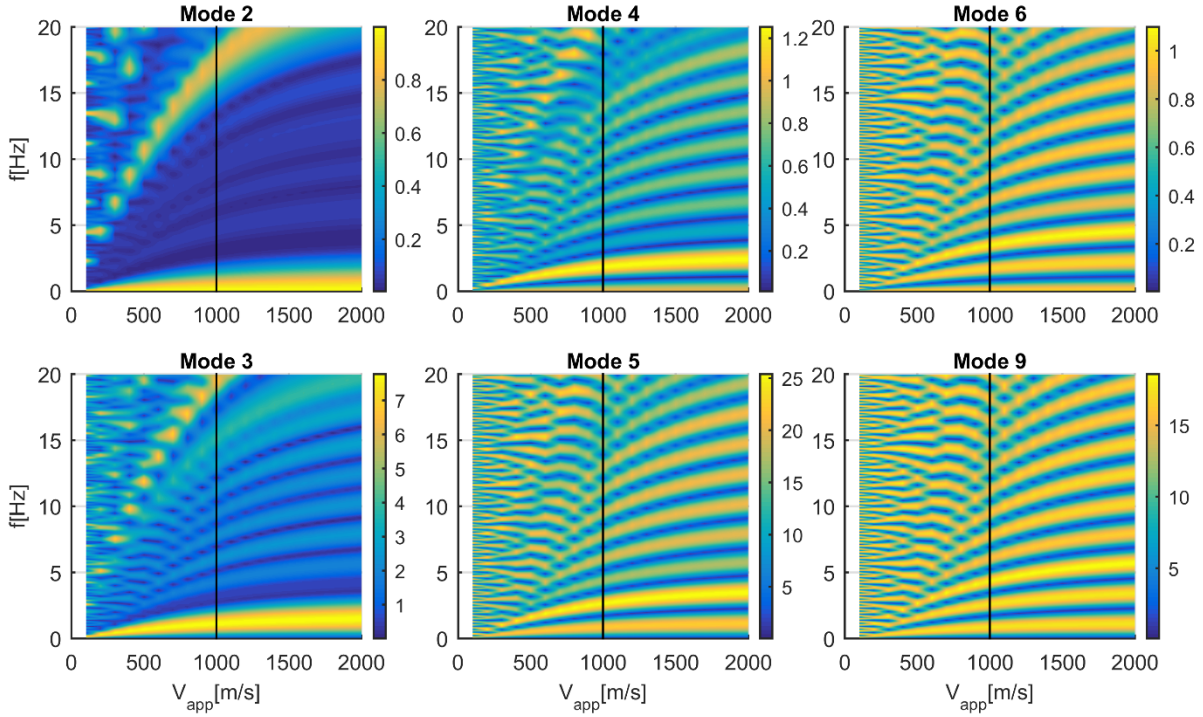

Figure 14: Scale factors $SF_i(\omega)$ for the Lissos bridge under the combined influence of the wave passage effect and the loss of coherency.

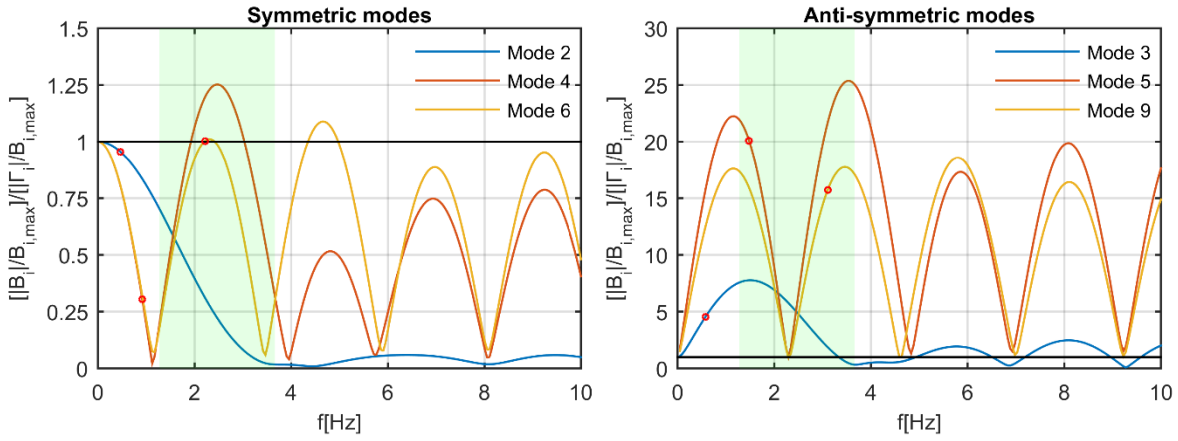

Figure 15: Scale factors $SF_i(\omega)$ (cross section of the surface graph of Fig.10) for the Lissos bridge under the wave passage effect.

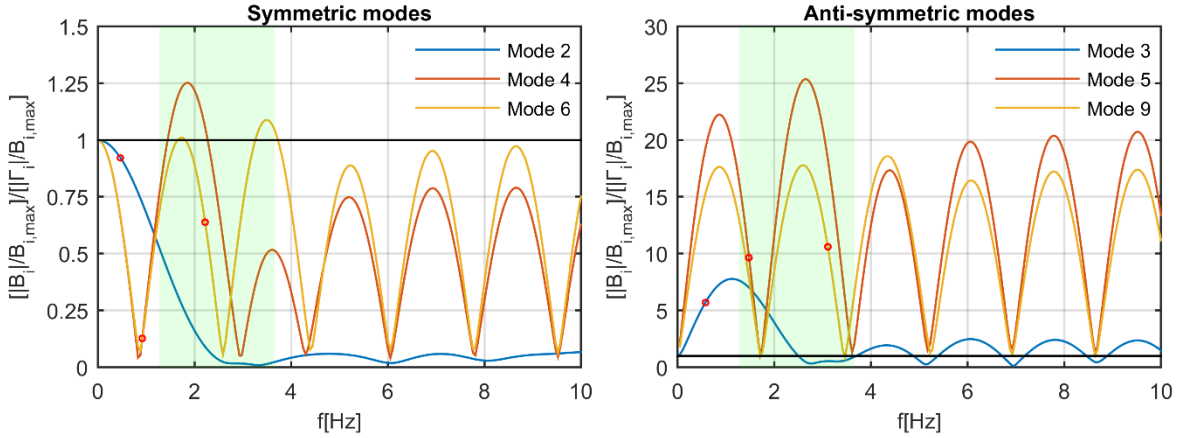

Figure 16: Scale factors $SF_i(\omega)$ (cross section of the surface graph of Fig.11) for the Lissos bridge under the combined influence of the wave passage effect and the loss of coherency.

In this context, Tables 4 and 5 summarize, for the Lissos and the Metsovo bridge respectively, the mean (μ_{SFi}) and the mean plus/minus standard deviation ($\mu_{SFi}\pm\sigma_{SFi}$) values of the scale factors $SF_i(\omega)$ estimated in the 1.273-3.66Hz range. Tables 4 and 5 additionally calculate the product of the out-of-the-parenthesis term of Eq.12. It is worth mentioning that only modes exhibiting $\mu_{SFi}>1$ or $\mu_{SFi}\pm\sigma_{SFi}>1$ (in the case of the $\mu_{SFi}\pm\sigma_{SFi}$ interval) are accounted for in the computation of $\left(\overline{SF_i}-1\right)\cdot\Gamma_i\cdot D_i$. The $\mathbf{F_i}$ forces were then statically applied to the structures and the resulting bending moments M_{Fi} were combined through the SRSS rule with those obtained from the conventional response spectrum analysis $M_{resp.spec.}$ according to Eq. 30.

Table 4: Scale factors $SF_i(\omega)$ & lateral forces F_i for Lissos bridge.

Mode	Γ_i	RSD x10^{-2} [m]	μ_{SF_i}	F_i [x$\left(\omega_i^2 \mathbf{M}\varphi_i\right)$]	$\mu_{SF_i} + \sigma_{SF_i}$	F_i [x$\left(\omega_i^2 \mathbf{M}\varphi_i\right)$]	$\mu_{SF_i} - \sigma_{SF_i}$	F_i [x$\left(\omega_i^2 \mathbf{M}\varphi_i\right)$]
Wave Passage Effect								
	(1)	(2)	(3)	(1)·(2)·(3-'1')	(4)	(1)·(2)·(4-'1')	(5)	(1)·(2)·(5-'1')
2	103.44	11.19	0.27		0.49		0.05	
3	-8.67	9.70	4.58	3.01	7.26	5.26	1.90	0.75
4	34.45	6.10	0.88		1.20	0.42	0.56	
5	-1.20	3.78	15.61	0.67	23.23	1.01	8.00	0.32
6	21.75	2.52	0.63		0.94		0.31	
9	0.97	1.45	11.65	0.15	17.11	0.23	6.20	0.07
Wave Passage Effect & Loss of Coherency								
	(1)	(2)	(3)	(1)·(2)·(3-'1')	(4)	(1)·(2)·(4-'1')	(5)	(1)·(2)·(5-'1')
2	103.44	11.19	0.13		0.29		0	
3	-8.67	9.70	2.66	1.40	5.23	3.55	0.09	
4	34.45	6.10	0.72		1.12	0.25	0.32	
5	-1.20	3.78	14.36	0.61	22.39	0.97	6.33	0.24
6	21.75	2.52	0.75		1.05	0.03	0.44	
9	0.97	1.45	9.87	0.12	15.42	0.20	4.33	0.05

Table 5: Scale factors $SF_i(\omega)$ & lateral forces F_i for Metsovo bridge.

Mode	Γ_i	RSD x10^{-2} [m]	μ_{SF_i}	F_i [x$\left(\omega_i^2 \mathbf{M}\varphi_i\right)$]	$\mu_{SF_i} + \sigma_{SF_i}$	F_i [x$\left(\omega_i^2 \mathbf{M}\varphi_i\right)$]	$\mu_{SF_i} - \sigma_{SF_i}$	F_i [x$\left(\omega_i^2 \mathbf{M}\varphi_i\right)$]
Wave Passage Effect								
	(1)	(2)	(3)	(1)·(2)·(3-'1')	(4)	(1)·(2)·(4-'1')	(5)	(1)·(2)·(5-'1')
1	-147.90	11.19	0.50		0.70		0.30	
3	5.36	11.19	11.68	6.40	13.94	7.75	9.41	5.04
6	-109.87	7.22	0.74		0.85		0.63	
12	-20.66	3.05	1.42	0.26	1.67	0.42	1.17	0.10
15	-51.89	2.25	0.70		0.78		0.62	
20	-12.50	1.25	1.26	0.04	1.79	0.12	0.74	
29	20.68	0.40	0.36		0.45		0.27	
30	-21.82	0.30	1.03	0.002	1.19	0.01	0.86	
46	-15.67	0.08	0.85		1.07	0.001	0.62	
47	-29.25	0.07	0.81		0.86		0.75	
Wave Passage Effect & Loss of Coherency								
	(1)	(2)	(3)	(1)·(2)·(3-'1')	(4)	(1)·(2)·(4-'1')	(5)	(1)·(2)·(5-'1')
1	-147.90	11.19	0.67		0.97		0.37	
3	5.36	11.19	10.33	5.59	13.27	7.36	7.38	3.83
6	-109.87	7.22	0.68		0.78		0.59	
12	-20.66	3.05	1.48	0.30	1.65	0.41	1.31	0.20
15	-51.89	2.25	0.66		0.75		0.58	
20	-12.50	1.25	1.30	0.05	1.71	0.11	0.90	
29	20.68	0.40	0.36		0.48		0.25	
30	-21.82	0.30	1.07	0.005	1.23	0.02	0.91	
46	-15.67	0.08	0.73		0.85		0.61	
47	-29.25	0.07	0.83		0.89		0.77	

Multi-support excitation effects were summarized through the impact mean ratios 'ϱ', already defined as the maximum seismic demand at each pier under differential support ground motion, over the respective one under identical input motion. Three ratios were computed for that purpose,

namely (a) μ_{SFi}, (b)$\mu_{SFi}+\sigma_{SFi}$, and (c) $\mu_{SFi}-\sigma_{SFi}$; these were estimated for all piers and ground motion scenarios considered, approaching the lateral $\mathbf{F}_i$ forces definition in a slightly modified manner. The ratio values along with the respective bending moments are summarized in Table 6 for the Lissos and Table 7 for the Metsovo bridge. Validation of the proposed approach is pursued in Section 5, where the results of Tables 6 and 7 are tested against the ones obtained through time history analysis with the use of partially correlated, spectrum-compatible input motions.

Table 6: Pier bending moments under uniform and non-uniform excitation for the Lissos bridge.

	P1	**P2**	**P3**	**P4**	**P5**	**P6**	**P7**	**P8**	**P9**	**P10**
					Uniform motion					
$M_{resp.spec}$ [MNm]	1.27	3.03	4.97	7.24	12.69	14.04	10.62	8.49	5.81	1.24
					Wave Passage Effect					
$M_{asynch.}$ (μ_{SF}) [MNm]	1.59	3.70	5.78	7.93	12.99	14.04	10.92	9.11	6.45	1.38
ϱ (μ_{SF})	*1.25*	*1.22*	*1.16*	*1.10*	*1.02*	*1.00*	*1.03*	*1.07*	*1.11*	*1.11*
$M_{asynch.}$ ($\mu_{SF}+\sigma_{SF}$) [MNm]	2.08	4.79	7.18	9.17	13.58	14.07	11.49	10.29	7.60	1.63
ϱ ($\mu_{SF}+\sigma_{SF}$)	*1.64*	*1.58*	*1.44*	*1.27*	*1.07*	*1.00*	*1.08*	*1.21*	*1.31*	*1.31*
$M_{asynch.}$ ($\mu_{SF}-\sigma_{SF}$) [MNm]	1.29	3.08	5.02	7.28	12.71	14.04	10.65	8.53	5.85	1.25
ϱ ($\mu_{SF}-\sigma_{SF}$)	*1.02*	*1.02*	*1.01*	*1.01*	*1.00*	*1.00*	*1.00*	*1.00*	*1.01*	*1.01*
					Wave Passage Effect & Loss of Coherency					
$M_{asynch.}$ (μ_{SF}) [MNm]	1.36	3.21	5.15	7.40	12.77	14.04	10.70	8.63	5.96	1.28
ϱ (μ_{SF})	*1.07*	*1.06*	*1.04*	*1.02*	*1.01*	*1.00*	*1.01*	*1.02*	*1.03*	*1.03*
$M_{asynch.}$ ($\mu_{SF}+\sigma_{SF}$) [MNm]	1.95	4.33	6.29	8.2	13.41	14.53	11.11	9.46	7.08	1.51
ϱ ($\mu_{SF}+\sigma_{SF}$)	*1.54*	*1.43*	*1.27*	*1.13*	*1.06*	*1.04*	*1.05*	*1.12*	*1.22*	*1.21*
$M_{asynch.}$ ($\mu_{SF}-\sigma_{SF}$) [MNm]	1.27	3.04	4.97	7.24	12.69	14.04	10.63	8.49	5.81	1.24
ϱ ($\mu_{SF}-\sigma_{SF}$)	*1.00*	*1.00*	*1.00*	*1.00*	*1.00*	*1.00*	*1.00*	*1.00*	*1.00*	*1.00*

Table 7: Pier bending moments under uniform and non-uniform excitation for the Metsovo bridge.

	P1	**P2**	**P3a**	**P3b**	**P1**	**P2**	**P3a**	**P3b**
				Uniform motion				
$M_{resp.spec}$ [MNm]	30.40	528.45	238.23	257.80	30.40	528.45	238.23	257.80
	Wave Passage Effect				**Wave Passage Effect & Loss of Coherency**			
$M_{asynch.}$ (μ_{SF}) [MNm]	35.60	534.78	249.07	260.54	37.11	528.45	238.23	257.80
ϱ (μ_{SF})	*1.17*	*1.01*	*1.05*	*1.01*	*1.22*	*1.01*	*1.03*	*1.01*
$M_{asynch.}$ ($\mu_{SF}+\sigma_{SF}$) [MNm]	42.57	538.04	253.98	261.82	42.07	537.29	252.48	261.43
ϱ ($\mu_{SF}+\sigma_{SF}$)	*1.40*	*1.02*	*1.07*	*1.02*	*1.38*	*1.02*	*1.06*	*1.01*
$M_{asynch.}$ ($\mu_{SF}-\sigma_{SF}$) [MNm]	31.28	532.33	245.00	259.50	33.55	530.73	242.17	258.79
ϱ ($\mu_{SF}-\sigma_{SF}$)	*1.03*	*1.01*	*1.03*	*1.01*	*1.10*	*1.00*	*1.02*	*1.00*

5. VALIDATION

5.1 Overview

Validation of the proposed approach was achieved with the use of time history analysis. In particular, the results obtained for the two bridges through the simplified approach (Section 4, response spectrum analysis plus a set of static analyses) are now compared with the ones estimated

through time history analysis considering partially correlated motions. The *m*-variate, fully non-stationary, spectrum-compatible ground motion vectors were constructed with the method of Cacciola & Deodatis [5]. For each bridge, twenty sets of thirty sample functions were generated for each direction of wave propagation (left to right and vice versa); in this context, a response sample corresponds to the mean response of a bridge subjected to 30 sample functions of partially correlated motions. Overall, a total set of 1,200 realizations (20 sets x 30 sample functions x 2 directions) of 12-variate, for the Lissos bridge, and 5-variate, for the Metsovo bridge, fully non-stationary, spectrum-compatible input motions were generated. Three excitation scenarios were examined as previously: (a) synchronous excitation due to input motion generated at abutment Ab_1 (or Ab_2), (b) asynchronous excitation due to finite propagation velocity V_{app} using input motion generated at abutment Ab_1 (or Ab_2), and (c) asynchronous excitation due to incoherent input motion using the 600 simulated input motion sets (in each direction). Conclusively, a total set of 3,600 analyses (= (600 synchronous + 600 asynchronous due to V_{app} + 600 asynchronous due to V_{app} and loss of coherency) x 2 directions) were performed for each bridge using the direct integration method (integration step = 0.01sec).

Comparison of the results is made on the basis of the SVEGM impact mean ratios 'ϱ'; already defined as the maximum seismic demand at each pier (base bending moments) under asynchrnous support ground motion, over the respective EDP under uniform input motion.

5.2 Generation of input motions

Generation of the *m*-variate, fully non-stationary, spectrum-compatible ground motion vectors was based on the method of Cacciola & Deodatis [5]. The simulated ground motion vector process $f_j^{SC}(t)$ results from the superposition of two other processes ($f_j^{SC}(t) = f_j^{L}(t) + f_j^{C}(t)$): (a) a fully non-stationary process $f_j^{L}(t)$, with known cross-spectral density matrix $S^{L}(\omega,t)$ representing the desired geological and seismological conditions, and (b) a quasi-stationary corrective process $f_j^{C}(t)$, the cross-spectral density of which $S^{C}(\omega)$ has to be determined so that the simulated motions are spectrum-compatible.

More specifically, the method initiates with the definition of (a) the target response spectra $RSA^{(j)}$ at each location *j*, and (b) the evolutionary cross-spectral density matrix of the fully non-stationary $f_j^{L}(t)$ process, obtained through one of the methodologies provided in the literature (e.g. [26]). In the case the averaged simulated response spectra at each location *j* are not spectrum compatible, they are scaled by factor 'α_j' so as to match the respective targeted response spectrum in at least

one frequency, while all other spectral values remain lower than the targeted ones. The PSD function of the corrective process $G^C(\omega)$ ($=2S^C(\omega)$, $\omega \geq 0$; $=0$ elsewhere) is then calculated through a recursive procedure described in [5] and [2] and further improved through an iterative process until the simulated time histories' response spectra match the targeted ones according to the criteria set.

After the power spectrum density $S^C(\omega)$ of the quasi-stationary corrective process $f_j^C(t)$ has been determined, the evolutionary power spectrum of the simulated motions is given by:

$$S_{jj}^{SC}(\omega,t) = a_j^2 S_{jj}^{L}(\omega,t) + \varphi_j^2(t)\, S_{jj}^{C}(\omega) \tag{31}$$

$$S_{jk}^{SC}(\omega,t) = \sqrt{S_{jj}^{SC}(\omega,t)\, S_{kk}^{SC}(\omega,t)}\,\Gamma_{jk}(\omega) \tag{32}$$

where $\varphi(t)$ is the selected modulating function and $\Gamma_{jk}(\omega)$ is the selected coherency model. The ground motion sample functions at different locations can be derived as [26]:

$$f_j(t) = 2\sum_{r=1}^{m}\sum_{s=1}^{N}\left|H_{jr}(\omega_s,t)\right|\sqrt{\Delta\omega}\cos\left[\omega_s t - \arctan\left(\frac{\mathrm{Im}\left[H_{jr}(\omega_s,t)\right]}{\mathrm{Re}\left[H_{jr}(\omega_s,t)\right]}\right) + \varphi_{rs}\right] \tag{33}$$

where $H_{jr}(\omega_s,t)$ is the lower triangle of the Cholesky decomposition of the evolutionary power spectrum $S^{SC}(\omega,t)$ and φ_{rs} is an independent phase angle, uniformly distributed within [0, 2π].

The Clough & Penzien [72] acceleration power spectrum was selected to represent the cross spectral matrix of the "known" fully non-stationary process:

$$S_{jj}^{L}(\omega,t) = A(t)^2\, S_o \frac{\left(1+4\zeta_g^2(t)\left(\frac{\omega}{\omega_g(t)}\right)^2\right)}{\left(1-\left(\frac{\omega}{\omega_g(t)}\right)^2\right)^2 + 4\zeta_g^2(t)\left(\frac{\omega}{\omega_g(t)}\right)^2} \frac{\left(\frac{\omega}{\omega_f(t)}\right)^4}{\left(1-\left(\frac{\omega}{\omega_f(t)}\right)^2\right)^2 + 4\zeta_f^2(t)\left(\frac{\omega}{\omega_f(t)}\right)^2} \tag{34}$$

where $\omega_g(t)$ and $\zeta_g(t)$ are the frequency and the damping ratio of the ground at point *j*, while $\omega_f(t)$ and $\zeta_f(t)$ are the respective filtering parameters. The acceleration intensity is given by [5]:

$$S_0(t) = \frac{\sigma^2}{\pi\omega_g(t)\left(2\zeta_g(t) + \frac{1}{2\zeta_g(t)}\right)} \tag{35}$$

while the Bogdanoff-Goldberg-Bernard modulating function $A(t) = a_1 te^{(-a_2 t)}$ was utilized. The values of these variables were considered to be equal to the ones used by Cacciola & Deodatis [5], i.e. the standard deviation of the Kanai-Tajimi part of the spectrum σ=100cm/s^2 as well as the other parameters $\omega_g(t)$=20-7t/30rad/s, $\zeta_g(t)$= 0.6-0.2t/30rad/s, $\omega_f(t)$=0.10$\omega_g(t)$ and $\zeta_f(t)$=$\zeta_g(t)$. The Harichandran & Vanmarcke coherency model [79] was selected for this study, with the use of the parameters estimated by Harichandran & Wang [80] when analyzing the data of the SMART-1 array, that is A=0.626, α=0.022, k=19700m, ω_o=12.692rad/s and b=3.47:

$$\gamma_{jk}(\omega) = A\exp\left[-\frac{2\xi_{jk}}{a\theta(\omega)}(1-A+aA)\right] + (1-A)\exp\left[-\frac{2\xi_{jk}}{a\theta(\omega)}(1-A+aA)\right] \tag{36}$$

$$\theta(\omega) = k\left[1+\left(\frac{\omega}{\omega_o}\right)^b\right]^{-0.5} \tag{37}$$

The reason for the selection of this model instead of the one proposed by Luco & Wong (which the simplified approach is based on) is twofold: (a) contrary to the Luco & Wong model, the Harichandran & Vanmarcke coherency model exhibits partial correlations at the low frequencies, ensuring that no numerical problems will arise during the Cholesky decomposition of the cross spectral density matrix [8], and (b) the Harichandran & Vanmarcke coherency model does not exhibit a sharp exponential decay with separation distance and frequency, leading to a higher contribution of the dynamic component in bridges' total response [81,82]. In addition, since the set of ground motions generated by the Harichandran & Vanmarcke model exhibits a higher correlation degree compared to the Luco & Wong model, comparison of the results between the two methods (simplified approach and time history analysis) is bound to be risk adverse.

The upper cut-off frequency ω_u for the simulation of the "known" vector process $f_j^L(t)$ was set to 125.66rad/s (=20Hz), while the frequency step was defined as $\Delta\omega = \omega_u/N$ (N=1048). In total, 2048 time instances were used in the simulation, with the time step equal to 0.01s.

Having obtained a pertinent representation of the "known" vector process, the averaged simulated response spectra at each location j were calculated and compared with the targeted ones. The target

spectra were the Type 1 elastic response spectra provided by EC8 for soil class A. The recursive procedure for the estimation of the power spectral density function of the corrective process was then performed. At the next stage, in order for the evolutionary power spectrum to be determined, the modulating function $\varphi(t)$ proposed by Jennings, Housner and Tsai [83] was used:

$$\varphi(t)=\begin{cases}(t/t_1)^2 & t<t_1\\ 1 & t_1\le t\le t_2\\ \exp\left(-\beta\left(t-t_2\right)\right) & t>t_2\end{cases} \tag{38}$$

where t_1 and t_2 are calculated through the extension of the Husid function to the stochastic processes:

$$E_L^{(j)}(t)=\frac{\int_0^t\int_0^\infty S_{jj}^L(\omega,t)\,d\omega dt}{\int_0^{t_f}\int_0^\infty S_{jj}^L(\omega,t)\,d\omega dt} \tag{39}$$

and the coherency model used is the same one initially considered. The scaled cross spectral matrix of the "known" process $f_j^L(t)$, the power spectral density function of the corrective process $f_j^C(t)$ and the final evolutionary PSD at support point P4 for the case of soil B, PGA=0.24g, V_{app}=1500m/s are illustrated in Fig. 17. Finally, the ground motion sample functions at different locations were generated through the process of Deodatis [26], without the need for further iterations. A typical sample function set of the accelerograms at each bridge support for the case of soil A, PGA=0.16g and V_{app}=1000m/s is illustrated in Fig. 18. Convergence of the mean spectra of the thirty sample functions generated for this combination of soil and PGA (A-0.16g) to the targeted spectra is illustrated in Fig. 19.

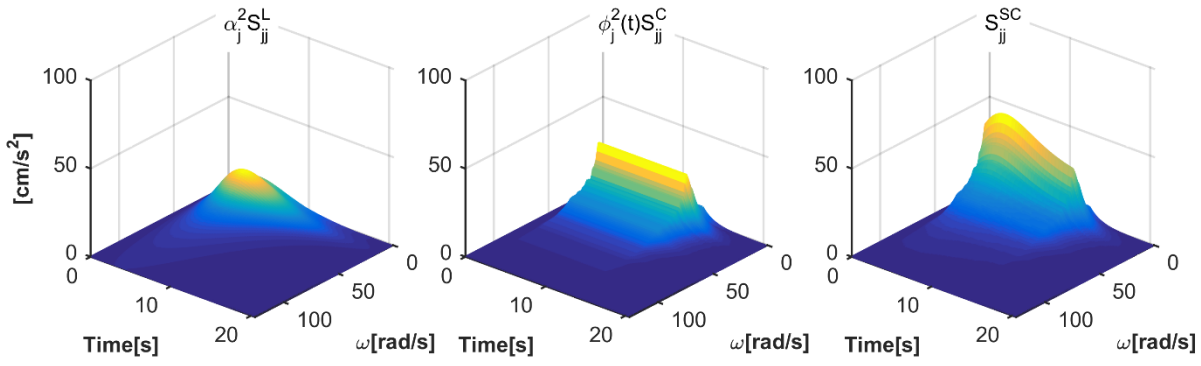

Figure 17: Scaled cross spectral matrix $S^L(\omega,t)$ of the "known" process $f_j(t)$ (left), the power spectrum density $S^C(\omega)$ of the corrective process $f_j(t)$ (in the middle) and the final evolutionary PSD at support point P6 for the case of soil A, PGA=0.16g, V_{app}=1000m/s.

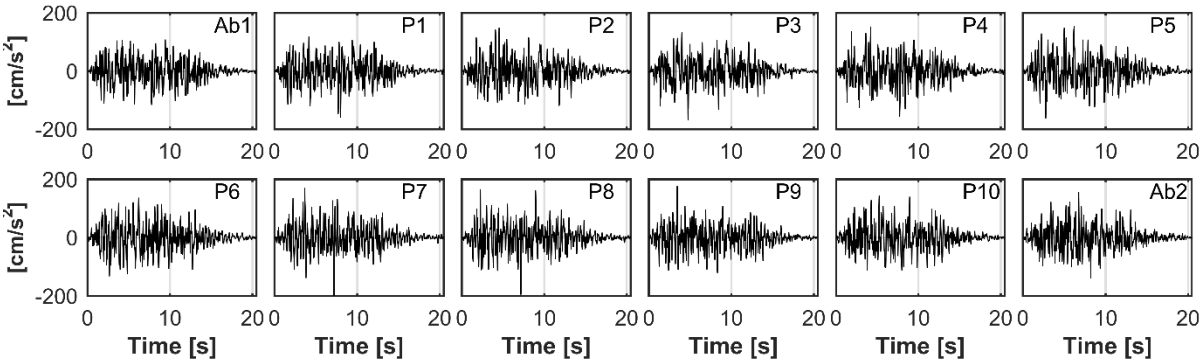

Figure 18: Typical set of accelerograms along the Lissos bridge supports for the case of soil A, PGA=0.16g, V_{app}=1000m/s.

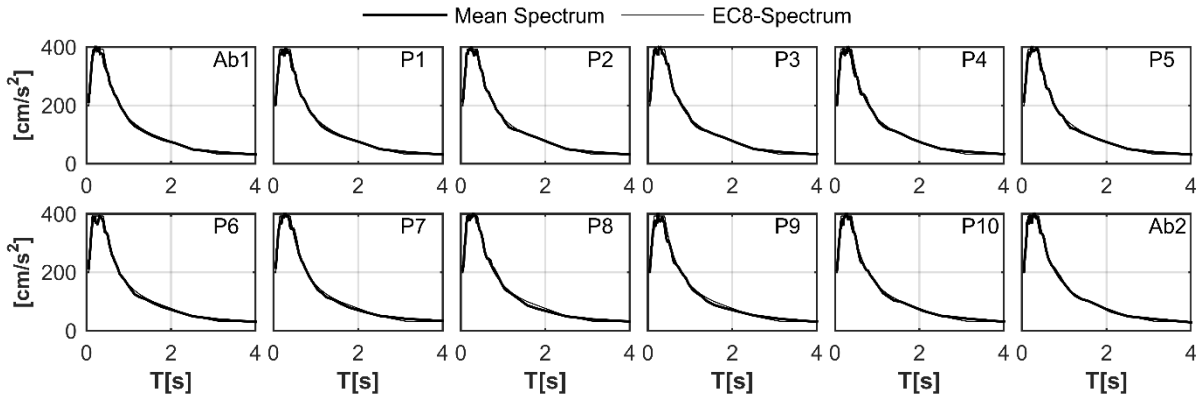

Figure 19: Comparison of the mean response spectra (30 realizations) of the generated motions for the case of soil A, PGA=0.16g, V_{app}=1000m/s.

5.3 Comparison of the results

In terms of the time history analysis, the mean 'ϱ' for each set (20 sets in total) of thirty sample functions of ground motion in each direction was initially estimated at each pier. Then, the mean and the standard deviation of the aforementioned 20-set mean 'ϱ' were calculated for both directions. Their envelopes (maximum values between the directions) are presented in Fig. 20 and 21 for the Lissos and the Metsovo bridges respectively. In the same figures, the ratios 'ϱ' obtained through the triple application of the simplified approach (reffering to absolute response quantities-not mean) for (a) μ_{SFi}, (b) $\mu_{SFi}+\sigma_{SFi}$, and (c) $\mu_{SFi}-\sigma_{SFi}$ are also embedded. A first, quantitative observation that can be derived from the figures refers to the shape of the simplified process's curves: these are found to match well to that of the time history analysis for both bridges and in both cases whether the loss of coherency has been accounted for or not. A detailed comparison of the results illustrated in Fig. 20 and 21 is made in Tables 8 and 9 for the Lissos and the Metsovo bridges respectively. These tables present the mean ϱ_{μ} and the mean plus/minus the standard

deviation $\varrho_{\mu\pm\sigma}$ ratios estimated by the time history analyses along with the respective ratios computed by the simplified approach using either the mean $\varrho_{(\mu_{SF})}$ or the mean plus/minus standard deviation $\varrho_{(\mu_{SF}\pm\sigma_{SF})}$ scale factors for the modal participation factor. Validation of the effectiveness of the simplified approach is pursued through the percentage difference of the ϱ_{μ} and $\varrho_{(\mu_{SF})}$ ratios.

For the Lissos bridge (Fig.20 and Table 8), in the case when only the wave passage effect is taken into account, the difference between $\varrho_{(\mu_{SF})}$ and ϱ_{μ} is less than 5% in five out of the ten piers, the highest difference being -9.56% at pier P4. It must be noted that, if the mean plus/minus standard deviation scale factor for the modal participation factors is to be used, the results of the $\varrho_{(\mu_{SF}+\sigma_{SF})}$ simplified approach envelope those of the time history analysis with the risk of being over-conservative. Being safety-favorable, ratios 'ϱ' of the simplified approach always exceed unity, contrary to, for example, the time history analysis mean ratio for pier P6 equal to 0.94. When the loss of coherency is additionally considered in the time history analysis framework, the detrimental effects appear to exhibit a decreasing trend except for piers P1 & P10, located next to the abutments; these piers seem to have the largest differences between the $\varrho_{(\mu_{SF})}$ and ϱ_{μ} ratios (-27.37% and -20.27% respectively), while, once again, the difference between these ratios is less than 5% in five out of the ten piers. It must be noted that, if the mean plus/minus standard deviation scale factor for the modal participation factors is to be used, the results of the $\varrho_{(\mu_{SF}\pm\sigma_{SF})}$ simplified approach envelope, except for pier P10, match those of the time history analysis without being excessively conservative, as in the case when only the wave passage effect is considered.

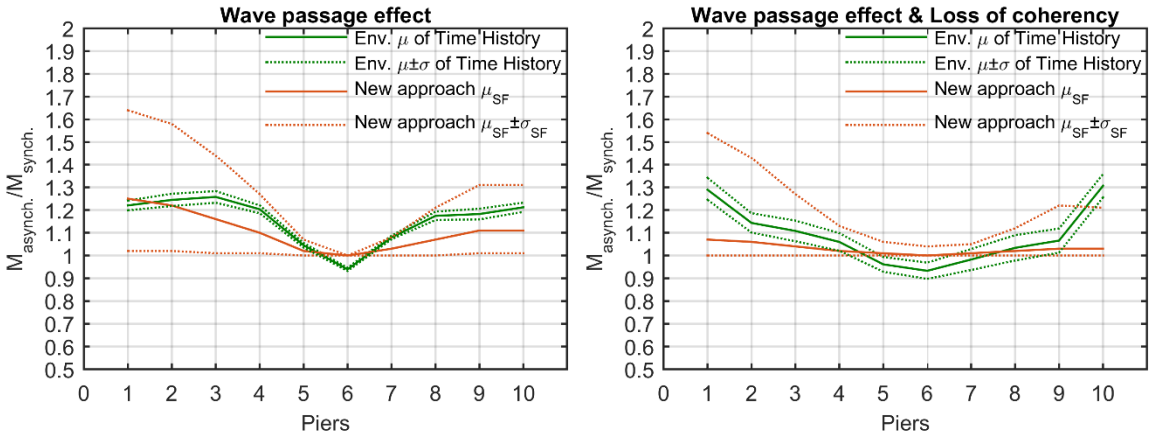

Figure 20: Ratios 'ϱ' of the seismic bending moments under SVEGM over synchronous excitation in the case of the Lissos bridge.

Table 8: Comparison between the THA and the simplified approach's ratios 'ϱ' in the case of the Lissos bridge. The arrows indicate each pier's critical direction of motion during the THA.

	Wave propagation effect									
	P1	**P2**	**P3**	**P4**	**P5**	**P6**	**P7**	**P8**	**P9**	**P10**
	←	←	←	←	←	→	→	→	→	→
Time history analysis										
ϱ_{μ}	1.22	1.24	1.26	1.20	1.05	0.94	1.08	1.17	1.18	1.21
$\varrho_{\mu\pm\sigma}$	1.20-1.24	1.22-1.27	1.23-1.28	1.19-1.22	1.03-1.06	0.93-0.95	1.07-1.09	1.16-1.19	1.16-1.21	1.19-1.23
Simplified approach										
$\varrho_{(\mu_{SF})}$	1.25	1.22	1.16	1.10	1.02	1.00	1.03	1.07	1.11	1.11
$\varrho_{(\mu_{SF}\pm\sigma_{SF})}$	1.02-1.64	1.02-1.58	1.01-1.44	1.01-1.27	1.00-1.07	1.00-1.00	1.00-1.08	1.00-1.21	1.01-1.31	1.01-1.31
Comparison										
$\frac{\varrho_{(\mu SF)} - \varrho_{\mu}}{\varrho_{(\mu SF)}}$	2.43%	-1.64%	-8.23%	-9.56%	-2.56%	6.04%	-5.05%	-8.94%	-6.28%	-8.77%
	Wave propagation effect & loss of coherency									
	P1	**P2**	**P3**	**P4**	**P5**	**P6**	**P7**	**P8**	**P9**	**P10**
	←	→	→	→	→	←	←	←	←	→
Time history analysis										
ϱ_{μ}	1.29	1.14	1.11	1.06	0.96	0.93	0.98	1.03	1.07	1.31
$\varrho_{\mu\pm\sigma}$	1.25-1.34	1.10-1.19	1.06-1.15	1.02-1.10	0.93-0.99	0.90-0.97	0.94-1.03	0.98-1.09	1.01-1.12	1.26-1.36
Simplified approach										
$\varrho_{(\mu_{SF})}$	1.07	1.06	1.04	1.02	1.01	1.00	1.01	1.02	1.03	1.03
$\varrho_{(\mu_{SF}\pm\sigma_{SF})}$	1.00-1.54	1.00-1.43	1.00-1.27	1.00-1.13	1.00-1.06	1.00-1.04	1.00-1.05	1.00-1.15	1.00-1.22	1.00-1.21
Comparison										
$\frac{\varrho_{(\mu SF)} - \varrho_{\mu}}{\varrho_{(\mu SF)}}$	-20.27%	-7.88%	-6.96%	-3.64%	4.60%	7.02%	2.74%	-1.31%	-4.21%	-27.37%

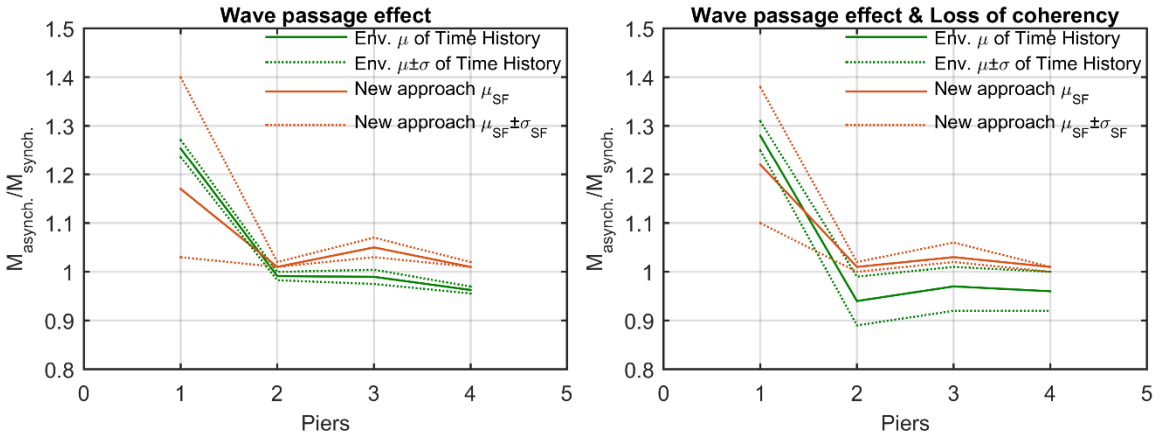

Figure 21: Ratios 'ϱ' of the seismic bending moments under SVEGM over synchronous excitation in the case of the Metsovo bridge.

Table 9: Comparison between the THA and the simplified approach's ratios 'ϱ' in the case of the Metsovo bridge. The arrows indicate each pier's critical direction of motion during the THA.

	Wave propagation effect				Wave propagation effect & Loss of Coherency			
	P1	**P2**	**P3a**	**P3b**	**P1**	**P2**	**P3a**	**P3b**
	→	←	←	←	→	←	←	←
Time history analysis								
ϱ_{μ}	1.25	0.99	0.99	0.96	1.27	0.94	0.97	0.96
$\varrho_{\mu\pm\sigma}$	1.24-1.27	0.98-1.00	0.97-1.00	0.96-0.97	1.25-1.31	0.89-0.99	0.92-1.01	0.92-1.00
Simplified approach								
$\varrho_{(\mu_{SF})}$	1.17	1.01	1.05	1.01	1.22	1.01	1.03	1.01
$\varrho_{(\mu_{SF}\pm\sigma_{SF})}$	1.03-1.40	1.01-1.02	1.03-1.07	1.01-1.02	1.10-1.38	1.00-1.02	1.02-1.06	1.00-1.01
Comparison								
$\frac{\varrho_{(\mu SF)} - \varrho_{\mu}}{\varrho_{(\mu SF)}}$	-6.73%	2.17%	5.31%	5.01%	-4.04%	6.87%	6.27%	4.77%

The simplified approach appears to adequately capture the response of the Metsovo bridge as well (Fig. 21 and Table 9). The THA results indicate the SVEGM effect to be marginally beneficial at all piers except for pier P1. Despite the simplified approach's ratios being always higher than unity, these vary from 1.01 to 1.05 for the P2, P3a, P3b piers, which are not vulnerable to the SVEGM, and are thus not considered to be overly conservative. In addition, for these piers, the $\varrho_{(\mu_{SF})}$ simplified approach curve is similar to the ϱ_{μ} time history analysis curve. As for pier P1, the differences between the $\varrho_{(\mu_{SF})}$ and ϱ_{μ} ratios are -4.04% and -6.73% when the loss of coherency is accounted for or not respectively. Similar to the Lissos bridge, if the mean plus/minus standard deviation scale factor of the modal participation factors is to be used, the results of the $\varrho_{(\mu_{SF}\pm\sigma_{SF})}$ simplified approach envelope those of the time history analysis with the risk of being over-conservative, especially in the case of pier P1.

It is important to note that the range of the simplified approach results (red lines in Fig.20 & 21) depends on the selected scale factor SF_i; the latter varies rapidly with the excitation frequency (Fig. 13 & 14). A physical explanation for this variation, especially in the case of higher modes, lies in the fact that the SF_i is estimated under the assumption of monochromatic waves travelling along the bridge; when the wavelength of a monochromatic wave, which, assuming a specific V_{app}, changes quickly in relation to the excitation frequency, matches the shape of a mode i, the $SF_i(\omega)$ presents peak, while, when the wavelength is much larger than bridge's length the $SF_i(\omega)$ shows a minimum. This is illustrated in Fig.22, which presents the contribution of modes 3 and 4 of the

Lissos bridge under asynchronous excitation (only V_{app} is considered, but similar results are expected when considering both V_{app} and the coherency). The highest SF for mode 3 equals 7.8 and corresponds to the case when a monochromatic wave with excitation frequency $f_{excit.}$=1.51Hz travels with V_{app}=1000m/s. In this case, its waveform is almost a perfect match to the 3rd mode's shape (2nd column, 1st graph). Similarly, the highest SF for mode 4 equals 1.25 and corresponds to the case when a monochromatic wave with excitation frequency $f_{excit.}$=2.48Hz travels with V_{app}=1000m/s. In this case, its waveform is again an almost perfect match to the 4th mode's shape (2nd column, 6th graph). Contrary to the previous cases, when a monochromatic wave with $f_{excit.}$=1.12Hz travels with V_{app}=1000m/s, it cannot excite the 4th mode (2nd column, 5th graph).

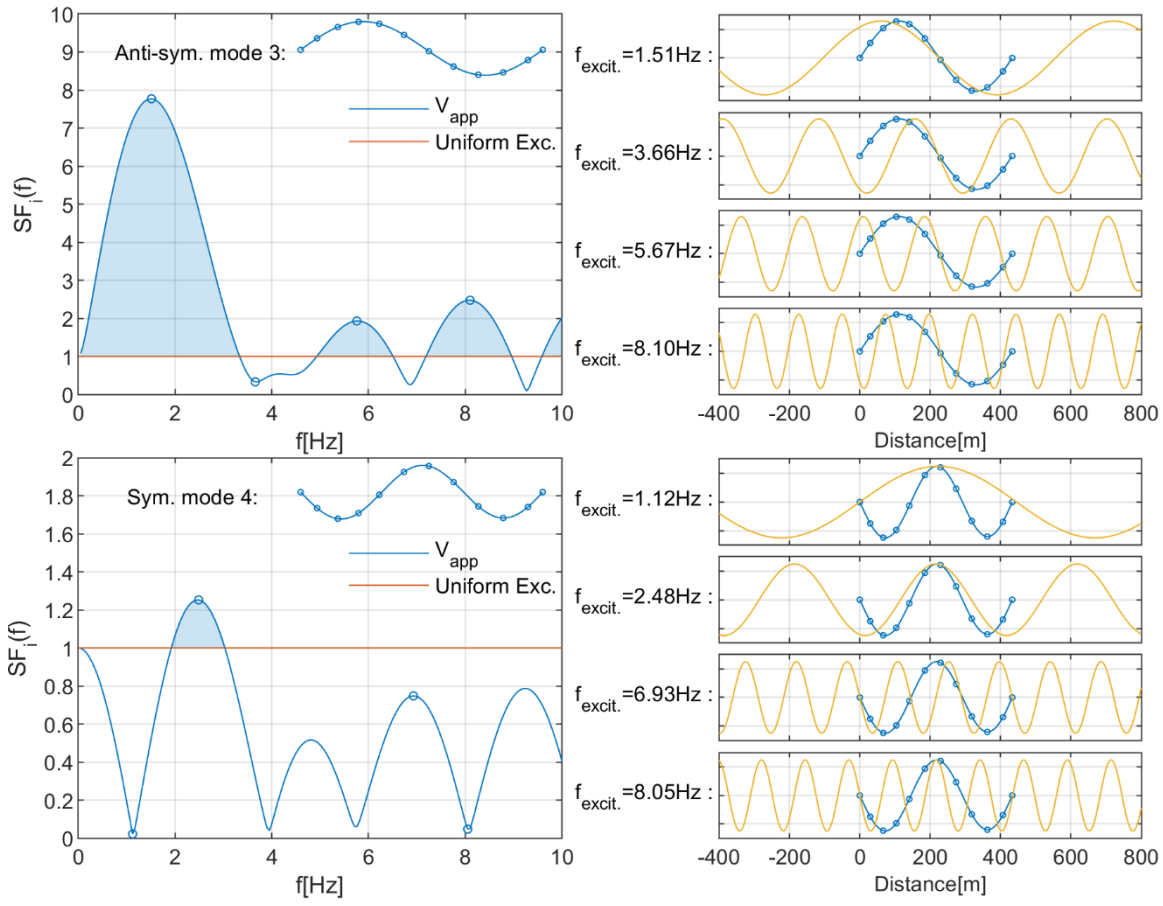

Figure 22: Interpretation variance of the scale factors $SF_i(\omega)$ with respect to the excitation frequency f (modes 3 and 4 of Lissos bridge under wave passage effect (V_{app}=1000m/s)). In the right column, the mode shapes are compared with monochromatic waveforms (yellow lines) under different frequencies.

Contrary to the results already presented where the THA ϱ_μ ratios envelope the means of the 20-set mean 'ϱ', the 600 (20 sets of 30 analyses each) bridge responses are now considered as a uniform sample space along each direction of motion. The ratios 'ϱ' that result from the 600 analyses for seismic wave propagation from Ab_1 (left) to Ab_2 (right) and vice versa are illustrated in Fig. 23 and

24 for the Lissos and Metsovo bridges respectively. These figures also illustrate the simplified approach's results while an overview of the two is presented in Tables 10 and 11. At this point it is important to note that none of the 600 results presented in Fig. 23 & 24 should be compared alone with the results obtained from the simplified approach. This is due to the fact that, the estimation of the dynamic response of a bridge subjected to multi-support excitation using time history analysis is performed in a Monte Carlo framework, which necessitates a significant number of sets of partially correlated motions.

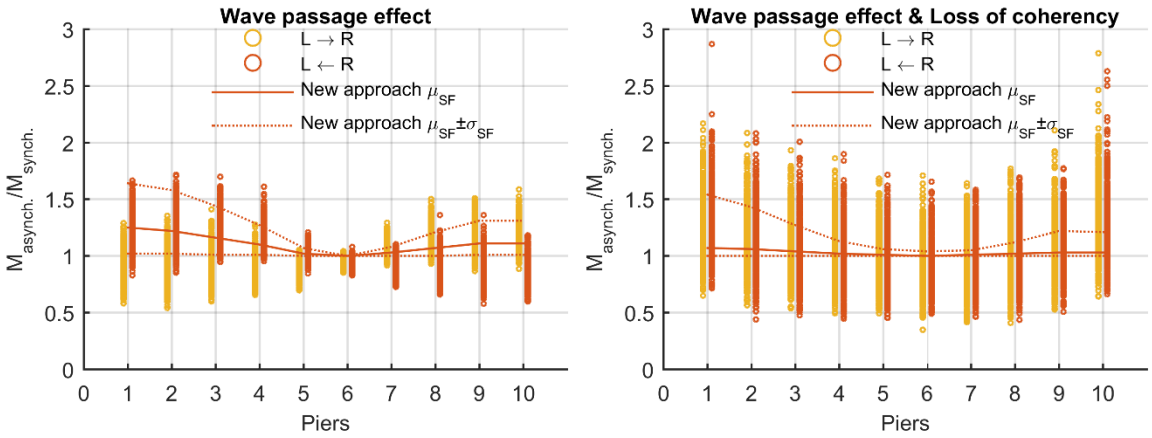

Figure 23: Comparison between the 600 THA for each direction of motion and the simplified approach's ratios of the seismic bending moments under SVEGM over synchronous excitation in the case of the Lissos bridge.

Table 10: Comparison between the THA and the simplified approach's ratios 'ϱ' in the case of the Lissos bridge. In THA, subscripts μ and σ are the maximum mean and the standard deviation of the response to 600 (= 20 set x 30 analyses) sample functions of ground motions between the two directions.

	Wave propagation effect									
	P1	**P2**	**P3**	**P4**	**P5**	**P6**	**P7**	**P8**	**P9**	**P10**
Time history analysis										
ϱ_{μ}	1.22	1.24	1.26	1.20	1.05	0.94	1.08	1.17	1.18	1.21
$\varrho_{\mu\pm\sigma}$	1.07-1.37	1.09-1.40	1.12-1.39	1.10-1.31	0.99-1.10	0.90-0.98	1.02-1.14	1.07-1.28	1.06-1.30	1.09-1.33
Simplified approach										
$\varrho_{(\mu_{SF})}$	1.25	1.22	1.16	1.10	1.02	1.00	1.03	1.07	1.11	1.11
$\varrho_{(\mu_{SF}\pm\sigma_{SF})}$	1.02-1.64	1.02-1.58	1.01-1.44	1.01-1.27	1.00-1.07	1.00-1.00	1.00-1.08	1.00-1.21	1.01-1.31	1.01-1.31
Comparison										
$\frac{\varrho_{(\mu SF)} - \varrho_{\mu}}{\varrho_{(\mu SF)}}$	2.43%	-1.64%	-8.23%	-9.56%	-2.56%	6.04%	-5.05%	-8.94%	-6.28%	-8.77%
	Wave propagation effect & loss of coherency									
	P1	**P2**	**P3**	**P4**	**P5**	**P6**	**P7**	**P8**	**P9**	**P10**
Time history analysis										

ϱ_{μ}	1.29	1.14	1.11	1.06	0.96	0.93	0.98	1.03	1.07	1.31
$\varrho_{\mu\pm\sigma}$	1.01-1.57	0.90-1.39	0.87-1.34	0.83-1.29	0.74-1.18	0.73-1.14	0.77-1.20	0.80-1.26	0.84-1.29	1.01-1.60
Simplified approach										
$\varrho_{(\mu_{SF})}$	1.07	1.06	1.04	1.02	1.01	1.00	1.01	1.02	1.03	1.03
$\varrho_{(\mu_{SF}\pm\sigma_{SF})}$	1.00-1.54	1.00-1.43	1.00-1.27	1.00-1.13	1.00-1.06	1.00-1.04	1.00-1.05	1.00-1.15	1.00-1.22	1.00-1.21
Comparison										
$\frac{\varrho_{(\mu SF)} - \varrho_{\mu}}{\varrho_{(\mu SF)}}$	-20.27%	-7.88%	-6.96%	-3.64%	4.60%	7.02%	2.74%	-1.31%	-4.21%	-27.37%

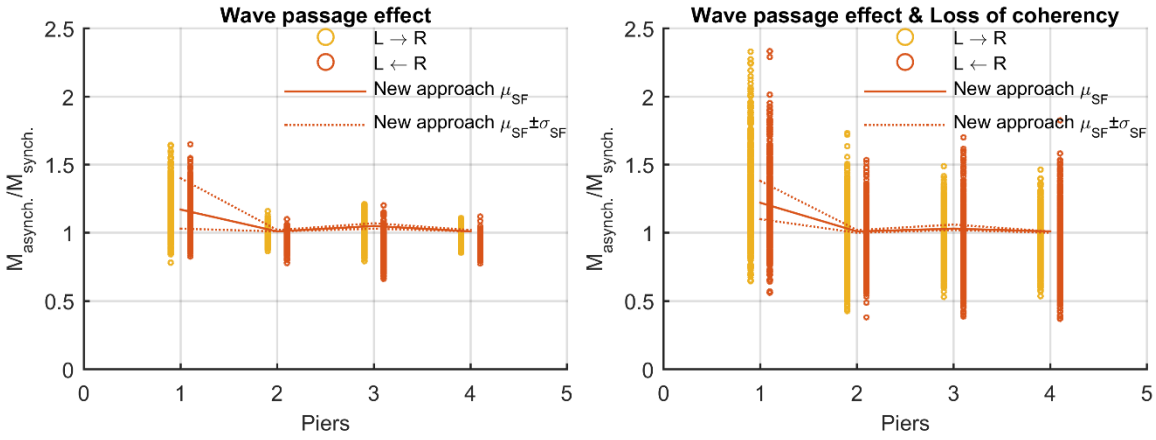

Figure 24: Comparison between the 600 THA for each direction of motion and the simplified approach's ratios of the seismic bending moments under SVEGM over synchronous excitation in the case of the Metsovo bridge.

Table 11: Comparison between the THA and the simplified approach's ratios 'ϱ' in the case of the Metsovo bridge. In THA, subscripts μ and σ are the maximum mean and the standard deviation of the response to 600 (= 20 set x 30 analyses) sample functions of ground motions between the two directions.

	Wave propagation effect				**Wave propagation effect & Loss of Coherency**			
	P1	**P2**	**P3a**	**P3b**	**P1**	**P2**	**P3a**	**P3b**
	→	←	←	←	→	←	←	←
Time history analysis								
ϱ_{μ}	1.25	0.99	0.99	0.96	1.27	0.94	0.97	0.96
$\varrho_{\mu\pm\sigma}$	1.16-1.35	0.95-1.03	0.92-1.06	0.92-1.00	1.11-1.42	0.69-1.18	0.80-1.14	0.79-1.13
Simplified approach								
$\varrho_{(\mu_{SF})}$	1.17	1.01	1.05	1.01	1.22	1.01	1.03	1.01
$\varrho_{(\mu_{SF}\pm\sigma_{SF})}$	1.03-1.40	1.01-1.02	1.03-1.07	1.01-1.02	1.10-1.38	1.00-1.02	1.02-1.06	1.00-1.01
Comparison								
$\frac{\varrho_{(\mu SF)} - \varrho_{\mu}}{\varrho_{(\mu SF)}}$	-6.73%	2.17%	5.31%	5.01%	-4.04%	6.87%	6.27%	4.77%

As expected, the mean ϱ_{μ} values equal those presented above for both bridges, while the range $(\varrho_{\mu-\sigma}, \varrho_{\mu+\sigma})$ increases. It is worth mentioning that, for each pier of both bridges, the $\varrho_{(\mu_{SF})}$ ratio of the simplified approach lies in the $(\varrho_{\mu-\sigma}, \varrho_{\mu+\sigma})$ range defined through time history analysis.

Time history analyses' results indicate that, at least in the case of the Lissos and Metsovo bridges, the simplified method presented herein offers an efficient means for the accurate representation of the SVEGM impact on bridge response. The use of the mean $SF_i(\omega)$ value plus a percentage of its standard variation is deemed a reasonable option that also avoids overconservatism. However, further investigation is needed in order for the best practice to be defined. Special attention should be paid to the fact that in the case of seismic isolated bridges, such as the Lissos bridge, there does not exist any simplified method (either in the EC8 or in the literature) that is able to capture the effects of multi-support excitation due to them being dependent upon the statically imposed displacements. However, the actual breakthrough and significant advantage of the proposed method over the other existing ones lies in the number of analyses required; 16 analyses (15 static analyses: 12 at Step 3 and 3 at Step 9, 1 response spectrum analysis at step10) in the case of the Lissos bridge and 11 analyses (10 static analyses: 15 at Step 3 and 5 at Step 9, 1 response spectrum analysis at step10) in the case of the Metsovo bridge were only performed.

Overall, despite the fact that refined methods are more appropriate for assessing the seismic response of complex bridges (e.g. cable-stayed ones), the simplified approach could be used as a preliminary test to estimate their sensitivity to SVEGM effects.

6. APPLICATION IN A SEISMIC CODE FRAMEWORK

The efficiency of the proposed method (as verified above) can presumably lead to a further simplified (code-oriented) version of seismic analysis, comprised of five (out of the eleven) aforementioned steps of the original method: Step 2 (Modal Analysis), Step 4 (Modal Participation Factor $\Gamma_{i,k}$), Step 9 (Static Analysis with Loading Forces F_i, eq. 29), Step 10 (Conventional Dynamic Analysis) and Step 11 (Design Quantities Superposition Rule). In such a case, the seismic code could potentially provide the required mean scale factor of higher mode excitation with respect to the type of the examined bridge and its configuration. For example, in the present applications, the required mean scale factor of higher mode excitation could indicatively be taken in the range of $SF_1(\omega)$=2.66-7.38 with $SF_2(\omega)=SF_1(\omega)/2$ for the first and the second anti-symmetric modes respectively. Therefore, the scale factors for these two modes can be estimated in the range described above (in the second case, the reason behind it is to avoid being over-conservative). For

all other modes the SFi(ω) could be reasonably taken equal to unity, effectively ignoring spatial variability on the grounds that it is beneficial for the overall structural response. Further research is needed to explore the range of variation of SFi(ω) for different structural typologies.

7. CONCLUSIONS

This paper presents a novel, bridge-dependent approach for the quantification of the effect of asynchronous earthquake ground motion. The method is reasonably simple and broadens the applicability of existing seismic code provisions to the case of seismic-isolated bridges, which are insensitive to the code-prescribed statically imposed displacements. Contrary to the existing methodologies which estimate the displacement patterns at bridge supports independently of bridge characteristics, this method examined the problem in an inverse manner: it is based on the assumption that if the effects of spatial variability are critical this is due to the excitation of higher modes of vibration and only locally affects the design quantities of specific components that are associated with these modes. This has been long identified in the literature but has never been employed in a design framework. Along these lines a set of arrows of spatially distributed lateral forces, whose patterns match the shape of the response-contributing anti-symmetric modes, are applied on the structure. The magnitude of those forces is based on the expected amplification of the anti-symmetric modes under the SVEGM, as they are quantified by Price & Eberhard [4].

Two real bridges were used as a test-bed to study the applicability and effectiveness of the proposed method; the Lissos bridge, a 11-span, base-isolated R/C structure, and the Metsovo bridge, a 4-span structure in which two (out of the three) piers are monolithically connected to the deck. The influence of multi-support excitation on the seismic demand was estimated on the basis of the SVEGM impact mean ratios 'ϱ', defined as the maximum seismic demand at each pier (base bending moments) under differential support ground motion, over the respective EDP under uniform input motion. The results from the simplified method presented herien were tested against the ones obtained through time history analysis; the latter made use of partially correlated, spectrum-compatible input motions generated through the Cacciola & Deodatis method. Comparison showed that, for the bridges studied, the simplified approach offered a very efficient means for the adequately accurate representation of the SVEGM impact on bridge response. It was also proven much less computationally-intensive compared to time history analysis; fifteen static and one response spectrum analyses and ten static and one response spectrum analyses were conducted for the Lissos and the Metsovo bridges respectively without any need for generating spatially variable ground motions with all the associated uncertainties introduced and propagating to the performance assessment. Overall, it is believed that the presented method solves an

important issue in bridge design in meaningful way that is physically justified, computationally efficient and simple enough to be employed in a seismic code design framework.

ACKNOWLEDGEMENTS

The first author would like to acknowledge funding by the Hellenic State Scholarships Foundation (IKY) and Siemens through the "Research Programs for Excellence IKY / Siemens" Grant, in the framework of the Hellenic Republic - Siemens Settlement Agreement. The work was also partially funded by the Horizon 2020 Program of the European Commission through grant MSCA-RISE-2015-691213-EXCHANGE-Risk.

REFERENCES

[1] Sextos AG, Pitilakis KD, Kappos AJ. Inelastic dynamic analysis of RC bridges accounting for spatial variability of ground motion, site effects and soil-structure interaction phenomena. Part 1: Methodology and analytical tools. Earthq Eng Struct Dyn 2003;32:607–27. doi:10.1002/eqe.241.

[2] Papadopoulos SP, Sextos AG. Anti-symmetric mode excitation and seismic response of base-isolated bridges under asynchronous input motion. Soil Dyn Earthq Eng 2018;113:148–61. doi:10.1016/j.soildyn.2018.06.004.

[3] Sextos AG, Karakostas C, Lekidis V, Papadopoulos S. Multiple support seismic excitation of the Evripos bridge based on free-field and on-structure recordings. Struct Infrastruct Eng 2015;11:1510–23. doi:10.1080/15732479.2014.977302.

[4] Price TE, Eberhard MO. Effects of Spatially Varying Ground Motions on Short Bridges. J Struct Eng 1998;124:948–55. doi:10.1061/(ASCE)0733-9445(1998)124:8(948).

[5] Cacciola P, Deodatis G. A method for generating fully non-stationary and spectrum-compatible ground motion vector processes. Soil Dyn Earthq Eng 2011;31:351–60. doi:10.1016/j.soildyn.2010.09.003.

[6] Elnashai AS, Mwafy AM. Seismic Response and Design. ICE Man Bridg Eng 2008:145–63. doi:10.1680/mobe.34525.

[7] Sextos AG, Kappos AJ. Evaluation of seismic response of bridges under asynchronous excitation and comparisons with Eurocode 8-2 provisions. Bull Earthq Eng 2009;7:519–45. doi:10.1007/s10518-008-9090-5.

[8] Zerva A. Spatial variation of seismic ground motions. CRC Press Taylor & Francis Group; 2009.

[9] Tzanetos, Elnashai, Hamdan, Antoniou. Inelastic Dynamic Response of RC Bridges Subjected to Spatial Non-Synchronous Earthquake Motion. Adv Struct Eng 2000;3:191–214. doi:10.1260/1369433001502148.

[10] Burdette NJ, Elnashai AS. Effect of asynchronous earthquake motion on complex bridges. II: Results and implications on assessment. J Bridg Eng 2008:166–72.

[11] Der Kiureghian A, Neuenhofer A. Response spectrum method for multi-support seismic excitations. Earthq Eng Struct Dyn 1992;21:713–40. doi:10.1002/eqe.4290210805.

[12] Perotti F. Structural response to non-stationary multiple-support random excitation. Earthq Eng Struct Dyn 1990;19:513–27. doi:10.1002/eqe.4290190404.

[13] Nuti C, Vanzi I. Influence of earthquake spatial variability on differential soil displacements and SDF system response. Earthq Eng Struct Dyn 2005;34:1353–74. doi:10.1002/eqe.483.

[14] Yamamura N, Tanaka H. Response analysis of flexible MDF systems for multiple-support seismic excitations. Earthq Eng Struct Dyn 1990;19:345–57. doi:10.1002/eqe.4290190305.

[15] Harichandran RS, Hawwari A, Sweidan BN. Response of Long-Span Bridges to Spatially Varying Ground Motion. J Struct Eng ASCE 1996;122:476–84. doi:10.1061/(ASCE)0733-9445(1996)122:5(476).

[16] Nazmy AS, Abdel-Ghaffar AM. Effects of ground motion spatial variability on the response of cable-stayed bridges. Earthq Eng Struct Dyn 1992;21:1–20. doi:10.1002/eqe.4290210101.

[17] Lin J., Zhang Y., Li Q., Williams F. Seismic spatial effects for long-span bridges, using the pseudo excitation method. Eng Struct 2004;26:1207–16. doi:10.1016/j.engstruct.2004.03.019.

[18] Konakli K, Der Kiureghian A. Extended MSRS rule for seismic analysis of bridges subjected to differential support motions. Earthq Eng Struct Dyn 2011;40:1315–35. doi:10.1002/eqe.1090.

[19] Harichandran RS. Spatial variation of earthquake ground motion, what is it, how do we model it, and what are its engineering implications. East Lansing, MI: 1999.
[20] Der Kiureghian A, Keshishian P, Halabian AM. Multiple support response spectrum analysis of bridges including the site-response effect & the MSRS code. Berkeley, CA:University of California: 1997.
[21] Trifunac MD, Todorovska MI. Response spectra for differential motion of columns. Earthq Eng Struct Dyn 1997;26:251–68. doi:10.1002/(SICI)1096-9845(199702)26:2<251::AID-EQE642>3.0.CO;2-B.
[22] Zembaty Z, Rutenberg A. Spatial reponse spectra and site amplification effects. Eng Struct 2002;24:1485–96. doi:10.1016/S0141-0296(02)00096-2.
[23] Trifunac MD, Gicev V. Response spectra for differential motion of columns paper II: Out-of-plane response. Soil Dyn Earthq Eng 2006;26:1149–60. doi:10.1016/j.soildyn.2006.05.009.
[24] Zembaty Z. Spatial seismic excitations and response spectra. ISET J Earthq Technol 2007;44:233–58.
[25] Liao S, Zerva A. Physically compliant, conditionally simulated spatially variable seismic ground motions for performance-based design. Earthq Eng Struct Dyn 2006;35:891–919. doi:10.1002/eqe.562.
[26] Deodatis G. Non-stationary stochastic vector processes: seismic ground motion applications. Probabilistic Eng Mech 1996;11:149–67. doi:10.1016/0266-8920(96)00007-0.
[27] Konakli K, Der Kiureghian A. Simulation of spatially varying ground motions including incoherence, wave-passage and differential site-response effects. Earthq Eng Struct Dyn 2012;41:495–513. doi:10.1002/eqe.1141.
[28] Yang J-N. Simulation of random envelope processes. J Sound Vib 1972;21:73–85. doi:10.1016/0022-460X(72)90207-6.
[29] Lavorato D, Bergami A V., Rago C, Ma H Bin, Nuti C, Vanzi I, et al. Seismic behaviour of isolated RC bridges subjected to asynchronous seismic input. COMPDYN 2017 - Proc 6th Int Conf Comput Methods Struct Dyn Earthq Eng 2017;1:2214–26. doi:10.7712/120117.5561.18104.
[30] Lavorato D, Fiorentino G, Bergami AV, Briseghella B, Nuti C, Santini S, et al. Asynchronous earthquake strong motion and RC bridges response. J Traffic Transp Eng (English Ed 2018;5:454–66. doi:10.1016/j.jtte.2018.06.001.
[31] Lavorato D, Fiorentino G, Bergami A V., Ma H Bin, Nuti C, Briseghella B, et al. Surface generation of asynchronous seismic signals for the seismic response analysis of bridges. COMPDYN 2017 - Proc 6th Int Conf Comput Methods Struct Dyn Earthq Eng 2017;1:2203–13. doi:10.7712/120117.5560.18098.
[32] Bi K, Hao H. Modelling and simulation of spatially varying earthquake ground motions at sites with varying conditions. Probabilistic Eng Mech 2012;29:92–104. doi:10.1016/j.probengmech.2011.09.002.
[33] Deodatis G. Simulation of ergodic multivariate stochastic processes. J Eng Mech 1996;122:778–87. doi:10.1061/(ASCE)0733-9399(1996)122:8(778).
[34] Gao Y, Wu Y, Li D, Liu H, Zhang N. An improved approximation for the spectral representation method in the simulation of spatially varying ground motions. Probabilistic Eng Mech 2012;29:7–15. doi:10.1016/j.probengmech.2011.12.001.
[35] Shinozuka M. Monte Carlo solution of structural dynamics. Comput Struct 1972;2:855–74. doi:10.1016/0045-7949(72)90043-0.
[36] Zerva A. Seismic ground motion simulations from a class of spatial variability models. Earthq Eng Struct Dyn 1992;21:351–61. doi:10.1002/eqe.4290210406.
[37] Shinozuka M, Deodatis G. Simulation of Stochastic Processes by Spectral Representation. Appl Mech Rev 1991;44:191. doi:10.1115/1.3119501.
[38] Shinozuka M, Deodatis G. Simulation of multi-dimensional Gaussian stochastic fields by spectral representation. Appl Mech Rev 1996;49:29–53. doi:10.1115/1.3101883.
[39] Hao H, Oliveira CS, Penzien J. Multiple-station ground motion processing and simulation based on smart-1 array data. Nucl Eng Des 1989;111:293–310. doi:10.1016/0029-5493(89)90241-0.
[40] Legrue J, Menun C. Simulation of nonstationary ground motions using wavelets. 13th World Conf. Earthq. Eng., Vancouver, Canada: 2004.
[41] Shields MD. Simulation of spatially correlated nonstationary response spectrum – compatible ground motion time histories. J Eng Mech 2014;141:04014161. doi:10.1061/(ASCE)EM.1943-7889.0000884.
[42] Cacciola P. A stochastic approach for generating spectrum compatible fully nonstationary earthquakes. Comput Struct 2010;88:889–901. doi:10.1016/j.compstruc.2010.04.009.
[43] Cacciola P, Zentner I. Generation of response-spectrum-compatible artificial earthquake accelerograms with random joint timefrequency distributions. Probabilistic Eng Mech 2012;28:52–8. doi:10.1016/j.probengmech.2011.08.004.
[44] Sextos A, Kappos AJ, Mergos P. Effect of soil-structure interaction and spatial variability of ground motion on irregular bridges: the case of the Krystallopigi bridge. Proc. 13th World Conf. Earthq. Eng., Vancouver, Canada: 2004.
[45] Lou L, Zerva a. Effects of spatially variable ground motions on the seismic response of a skewed, multi-span, RC highway bridge. Soil Dyn Earthq Eng 2005;25:729–40. doi:10.1016/j.soildyn.2004.11.016.

[46] Monti G, Pinto PE. Effects of Multi-support excitation on isolated bridges. In: Friedland I, Constantinou. M., editors. Proc. U.S.-Italy Work. Seism. Prot. Syst. Bridg., 1998, p. 225.
[47] Zanardo G, Hao H, Modena C. Seismic response of multi-span simply supported bridges to a spatially varying earthquake ground motion. Earthq Eng Struct Dyn 2002;31:1325–45. doi:10.1002/eqe.166.
[48] Lupoi A. The Response of Isolated Bridges Accounting for Spatial Variability of Ground Motion. J Earthq Eng 2009;13:814–34. doi:10.1080/13632460802645106.
[49] Pinto PE, Franchin P. Open Issues in the Seismic Design and Assessment of Bridges. In: Garevski M, Ansal A, editors. Earthq. Eng. Eur., vol. 17, Dordrecht: Springer Netherlands; 2010, p. 568. doi:10.1007/978-90-481-9544-2.
[50] Abdel Raheem S, Hayashikawa T, Dorka U. Spatial variation effects on seismic response control of calble-stayed bridges. 14h World Conf. Earthq. Eng., 2008, p. 1–11.
[51] Mwafy A, Kwon O, Elnashai A, Hashash Y. Wave Passage and Ground Motion Incoherency Effects on Seismic Response of an Extended Bridge. J Bridg Eng 2011;16:364–74.
[52] Yang Z, He L, Bielak J, Zhang Y, Elgamal A, Conte J. Nonlinear seismic response of a bridge site subject to spatially varying ground motion. 16th ASCE Eng. Mech. Conf., Seattle,WA, USA: 2003.
[53] CEN. European Standard EN 1998-2. Eurocode 8: Design of structures for earthquake resistance—Part 2: Bridges. Brussels: CEN: 2005.
[54] Monti G, Nuti C, Pinto PE. Nonlinear Response of Bridges under Multisupport Excitation. J Struct Eng 1996;122:1147–59. doi:10.1061/(ASCE)0733-9445(1996)122:10(1147).
[55] Shinozuka M, Saxena V, Deodatis G. Effect of spatial variation of ground motion on highway structures. Princeton, NJ: 2000.
[56] Lupoi A, Franchin P, Pinto PE, Monti G. Seismic design of bridges accounting for spatial variability of ground motion. Earthq Eng Struct Dyn 2005;34:327–48. doi:10.1002/eqe.444.
[57] Pinto P, Franchin P. Issues in the Upgrade of Italian Highway Structures. J Earthq Eng 2010;14:1221–52. doi:10.1080/13632461003649970.
[58] Harichandran RS, Wang W. Response of Simple Beam to Spatially Varying Earthquake Excitation. J Eng Mech 1988;114:1526–41. doi:10.1061/(ASCE)0733-9399(1988)114:9(1526).
[59] Harichandran RS, Wang W. Response of indeterminate two-span beam to spatially varying seismic excitation. Earthq Eng Struct Dyn 1990;19:173–87. doi:10.1002/eqe.4290190203.
[60] Ettouney M, Hapij A, Gajer R. Frequency-Domain Analysis of Long-Span Bridges Subjected to Nonuniform Seismic Motions. J Bridg Eng 2001;6:577–86. doi:10.1061/(ASCE)1084-0702(2001)6:6(577).
[61] Wang J, Carr A, Cooke N, Moss P. Wave-passage effect on the seismic response of long bridges. 2003 Pacific Conf. Earthq. Eng., 2003.
[62] Capatti MC, Carbonari S, Dezi F, Leoni G, Morici M, Silvestri F, et al. Effects of Non-Synchronous Ground Motion Induced by Site Conditions on the Seismic Response of Multi-Span Viaducts. 6th Int. Conf. Earthq. Geotech. Eng., Christchurch, New Zealand: 2015.
[63] Özcebe AG, Smerzini C, Bhanu V. Insights into the Effect of Spatial Variability of Recorded Earthquake Ground Motion on the Response of a Bridge Structure. J Earthq Eng 2018;0:1–27. doi:10.1080/13632469.2018.1453412.
[64] Dumanogluid AA, Soyluk K. A stochastic analysis of long span structures subjected to spatially varying ground motions including the site-response effect. Eng Struct 2003;25:1301–10. doi:10.1016/S0141-0296(03)00080-4.
[65] Crewe AJ, Norman JAP. Experimental modelling of multiple support excitations of long span bridges. 4th Int Conf Earthq Eng 2006.
[66] Johnson N, Ranf RT, Saiidi MS, Sanders D, Eberhard M. Seismic Testing of a Two-Span Reinforced Concrete Bridge. J Bridg Eng 2008;13:173–82. doi:10.1061/(ASCE)1084-0702(2008)13:2(173).
[67] Li X, Zhang D-Y, Yan W, Chen Y-J, Xie W-C. Shake-Table Test for a Typical Curved Bridge : Wave Passage and Local Site Effects. J Bridg Eng 2015:1–14. doi:10.1061/(ASCE)BE.1943-5592.0000643.
[68] Infrastrutture M. Norme Tecniche per le Costruzioni [Technical Standards for Construction]. Gazzetta Ufficiale della Repubblica Italiana. 29:(S.O. 30) (in Italian). Rome, Italy: Istituto Poligrafico e Zecca dello Stato; 2008.
[69] Chopra AK. Dynamics of Structures: Theory and applications to earthquake engineering. 3rd ed. Upper Saddle River, NJ: Prentice-Hall Inc; 2007.
[70] Nuti C, Biondi S, Vanzi I. Design actions for continuous deck bridges considering non synchronous earthquake motion. 5th Inernational Conf. Earthq. Geotech. Eng., Santiago, Chile: 2011.
[71] Falamarz-Sheikhabadi MR, Zerva A. Simplified Displacement Loading Patterns for Incorporation of Spatially Variable Ground Motions in Bridge Seismic Design Codes. J Bridg Eng 2017;22:04017010-1–14. doi:10.1061/(ASCE)BE.1943-5592.0001035.
[72] Clough RW, Penzien J. Dynamics of structures. Third Edit. Berkeley, CA: Computers & Structures,

Inc.; 2003.
[73] Luco JE, Wong HL. Response of a rigid foundation to a spatially random ground motion. Earthq Eng Struct Dyn 1986;14:891–908. doi:10.1002/eqe.4290140606.
[74] Nuti C, Vanzi I. Influence of earthquake spatial variability on differential soil displacements and SDF system response. Earthq Eng Struct Dyn 2005;34:1353–74. doi:10.1002/eqe.483.
[75] MATLAB 2015a, The MathWorks, Inc., Natick, Massachusetts, United States n.d.
[76] Kramer SL. Geotechnical earthquake engineering. Upper Saddle River, NJ: Prentice Hall; 1996.
[77] Stathopoulos S. Bridge Engineering in Greece. In: Chen WF, Duan L, editors. Handb. Int. Bridg. Eng., CRC Press Taylor & Francis Group; 2013.
[78] SAP2000 Integrated Software for Structural Analysis and Design,Computers and Structures Inc., Berkeley, California n.d.
[79] Harichandran RS, Vanmarcke EH. Stochastic Variation of Earthquake Ground Motion in Space and Time. J Eng Mech 1986;112:154–74. doi:10.1061/(ASCE)0733-9399(1986)112:2(154).
[80] Harichandran RS, Wang W. Effect of spatially varying seismic excitation on surface lifelines. 4th U.S. Natl. Conf. Earthq. Eng., Palm Springs: 1990.
[81] Zerva A, Ang A.-S, Wen YK. Development of differential response spectra for lifeline seismic analysis. Probabilistic Eng Mech 1986;1:208–18. doi:10.1016/0266-8920(86)90014-7.
[82] Zerva A. Seismic loads predicted by spatial variability models. Struct Saf 1992;11:227–43. doi:10.1016/0167-4730(92)90016-G.
[83] Jennings PC, Housner GW, Tsai NC. Simulated Earthquake Motions. 4th World Conf. Earthq. Eng., Santiago, Chile: 1969.